Doctoral Thesis

Theoretical and Computational Study of the Structure and Dynamics of Flowing Polymer melts at Interface

Sohdam Jeong

Department of Chemical Engineering

Graduate School of UNIST

2019

Theoretical and Computational Study of the Structure and Dynamics of Flowing Polymer melts at Interface

Sohdam Jeong

Department of Chemical Engineering

Graduate School of UNIST

Theoretical and Computational Study of the Structure and Dynamics of Flowing Polymer melts at Interface

A thesis/dissertation
submitted to the Graduate School of UNIST
in partial fulfillment of the
requirements for the degree of
Doctor of Philosophy

Sohdam Jeong

06/19/2019 of submission

Approved by

Advisor
Chunggi Baig

Theoretical and Computational Study of the Structure and Dynamics of Flowing Polymer melts at Interface

Sohdam Jeong

This certifies that the thesis/dissertation of Sohdam Jeong is approved.

06/19/2019

signature

Advisor: Chunggi Baig

signature

Hyunhyub Ko

signature

Sang Kyu Kwak

signature

So Youn Kim

signature

Jiseok Lee

signature

Han Gi Chae

Abstract

Flow behaviors of polymeric liquids have been widely utilized in the field of polymer rheology for characterization of material properties and for theoretical development of general constitutive models. In particular, it has been observed that structural and dynamical behaviors of polymers show distinctive features under confined environment (interface), compared with bulk polymers. However, despite many academic efforts, detailed molecular processes underlying interfacial polymeric materials are still unclear. This dissertation aims to elucidate the basic molecular characteristics of the structural and dynamic functions generally observed in bulk/interfacial polymer systems undergoing complicated flow conditions (including switch-on, steady state, and switch-off of external field), via atomistic nonequilibrium molecular dynamics (NEMD) simulations. Thus, main contributions of this doctoral dissertation are based on three major subjects: 1) interfacial chain dynamics of confined polymer melts under steady shear flow; 2) stress overshoot of polymer melts undergoing start-up shear flow; 3) stress relaxation of polymer melts upon cessation of steady shear flow.

In confined polymer system, interfacial slip plays a crucial role in a variety of fluid dynamics problems occurring in practical polymer processing, lubrication, adhesion, etc. Our results for confined sheared polymers identify three distinctive characteristic regimes, with regard to the degree of slip, and reveal the underlying molecular mechanisms for each regime. Moreover, we extend this finding to confined short-chain branched (SCB) and ring polymer systems with boundary solid walls, thus analyze in detail the effect of short branches and closed-loop conformation on the polymer structure and dynamics at the interface, in comparison with the linear polymer system.

When shear flow is initially imposed in equilibrium polymeric liquids at sufficiently high rates, stress overshoot, one of the important nonlinear rheological behaviors is commonly found: shear stress gradually increases with time, and reaches a maximum value, then decreases to attain steady-state value. To resolve conflicting studied results and investigate the molecular mechanisms regarding the overshoot, a thorough analysis has dedicated. Therefore, fundamental issues can be answered such as why/how the stress overshoot occurs. Furthermore, after the imposed external force field is turned off in steady flowing system, polymeric liquids relieve stress gradually via complex structural and rheological transitions. We demonstrate the molecular origins for the stress relaxation exhibited by flowing polymeric materials, also provide answers to most basic questions for well-known experimental observations of the stress relaxation.

Contents

List of Figures

Figure 4.1.6. (Top) Schematic illustration of the characteristic molecular mechanism of the interfacial chains at high flow fields and the probability distribution function (PDF) of the representative mesoscopic chain conformations [Stretched (S), Fold (F), Half-dumbbell (HD), Coil (C)] obtained by the Brightness analysis during a tumbling cycle for the linear and SCB PE systems. (Bottom) Snapshots of a selected interfacial chain, describing the representative tumbling mechanisms for the linear and the SCB polymers under strong flow.

Figure 4.1.7. Degree of slip and the associated characteristic molecular mechanisms. (Left) Variation of degree of slip (d_s) as a function of *Wi* number for the simulated C_{128} ring and linear polyethylene (PE) melts. The vertical lines separate the three (weak, intermediate, and strong) representative flow regimes with respect to d_s for each system. The error bars are smaller than the size of the symbols unless otherwise specified. (Right) Schematic description of the characteristic molecular mechanism(s) of interfacial ring chains for each flow regime. Here the loop is a chain section comprised of the atoms located over one atomic layer from the wall surface.

Figure 4.1.8. Plots of the ratio between the *xx* and *zz* components of interfacial gyration tensor $\mathbf{G}^{inf}$ (whose calculation involves only the chains that have their center-of-mass below 2.5 σ from the wall) for the simulated C_{128} ring and linear polyethylene (PE) melts. The superscript 'inf' in $\mathbf{G}^{inf}$ indicates 'interfacial'. The vertical lines separate the three characteristic flow regimes. The error bars are smaller than the size of the symbols unless otherwise specified.

Figure 4.1.9. Snapshots of a selected interfacial chain for describing the characteristic molecular mechanisms (loop wagging and loop migration) for the C_{400} ring system in the intermediate flow regime.

Figure 4.1.10. Probability distribution function (PDF) of the loop wagging and loop migration mechanisms exhibited by the interfacial chains (top panel) and the (reduced) loop migration velocity $V_{lm}^{*}\left(=V_{lm}\Big/\sqrt{\varepsilon_{CH_2}/m_{CH_2}}\right)$ along the chain (bottom panel) for the C_{400} ring PE melt in the intermediate flow regime. Here the PDF represents the number of interfacial chains exhibiting either the loop wagging or migration dynamics as normalized by the total number of interfacial chains. We also note that some interfacial chains do not reveal any of such loop dynamics and others show both loop wagging and migration dynamics.

Figure 4.1.11. Snapshots of a selected interfacial chain for describing the representative molecular mechanisms (parallel and vertical loop tumbling) exhibited by interfacial chains for the C_{400} ring system under strong flow fields, depending on the angle of the loop-section plane relative to the *x*-*z* interfacial plane (i.e., the loop plane aligns in parallel to the *x*-*z* (vorticity) and the *x*-*y* (shear) planes for the parallel and vertical loop tumbling, respectively). The red circles indicate the loop sections involved in tumbling dynamics.

Figure 4.1.12. Probability distribution of the angle (θ_{loop}) of the loop-section plane with respect to the

x-*z* plane.

Figure 4.1.13. Mutual penetration behaviors between interfacial ring chains under strong flow fields. (Top) Average number N_{penet} of penetrating interfacial chains per interfacial chain (top panel) and penetration time t_{penet} (bottom panel), as a function of shear rate for the C_{400} ring melt. Here t_{penet} (the average time-length for which the mutual penetration remains) was normalized by the total interfacial residence time [the average time-length for which an interfacial chain resides inside the interfacial region (within 2.5 σ from the wall surface)]. To compute N_{penet} and t_{penet}, we first analyzed the adsorbed area of individual interfacial chains on the wall. We then directly measured how many other interfacial chains are penetrated within the area. Since the mutual penetration between interfacial chains requires a closed space for a reference chain to trap other chains, it is a unique phenomenon for ring polymers bearing the intrinsic characteristic of a closed-loop conformation. Furthermore, this feature become larger with increasing chain length, because the closed surface area increases for longer ring chains; e.g., N_{penet} and t_{penet} for the C_{128} ring PE melt (not shown here) are found to be much smaller than those for the C_{400} ring PE melt. (Bottom) Snapshots of two selected interfacial chains for describing how the mutual penetration behavior occurs and evolves with time for the C_{400} ring melt under strong flow.

Figure 4.2.1. Transient behavior of stress $\boldsymbol{\sigma}$, birefringence **n**, and entanglement segment orientation **S** (eq. 4.1), as a function of strain for the simulated $C_{400}H_{802}$ polyethylene melt under start-up shear at four different flow strengths: $Wi_d = 18.6$ and $Wi_R = 4.57$ (dark yellow solid lines), $Wi_d = 92.8$ and $Wi_R = 22.9$ (dark green dashed lines), $Wi_d = 371$ and $Wi_R = 91.4$ (black dotted lines), and $Wi_d = 928$ and $Wi_R = 229$ (orange dashed-dotted lines). Lines and symbols in bottom panel represent the orientation tensor results calculated from the entanglement network obtained via the Z1-code based on the number of carbon atoms per entanglement strand (N_e) set to 68, respectively (see the text for details). All properties are normalized (as indicated by the tilde symbol) by their steady-state value.

Figure 4.2.2. (Top) Plot of birefringence n_{xy} versus shear stress σ_{xy} at four different flow strengths: $Wi_d = 18.6$ and $Wi_R = 4.57$ (dark yellow circles), $Wi_d = 92.8$ and $Wi_R = 22.9$ (dark green diamonds), $Wi_d = 371$ and $Wi_R = 91.4$ (black triangles), and $Wi_d = 928$ and $Wi_R = 229$ (orange squares). (Bottom) Plots of σ_{xy} (red solid lines), n_{xy} (dark yellow long-dashed lines), S_{xy} (eq. 4.1, black short-dashed lines), and $S_{xy}^{ee} = \langle u_{ee,x} u_{ee,y} \rangle$ (dark brown dotted lines, where $\mathbf{u}_{ee}$ is the unit chain end-to-end vector), as a function of strain for the simulated C_{400} PE melt under start-up shear at four different flow strengths; each property is normalized by its steady-state value. For comparison purposes, the corresponding result of L_{pp} (dark green dashed-dotted lines) is also shown in each plot.

Figure 4.2.3. (Top) Angular probability distribution function $P(\theta)$ for the chain orientation angle θ. Here, θ was computed based on the chain center-to-center vector (connecting two centers of mass of the bisected chain), which was shown to more precisely describe the rotational dynamics of individual

chains in comparison with the chain end-to-end vector. (Bottom) Distribution of shear stress $\sigma_{xy}^{\text{inter}}$ and the first normal stress difference N_1^{inter} contributed solely by the intermolecular LJ interactions between chains with respect to θ as a function of strain.

Figure 4.2.4. Schematic illustration of the overall characteristic molecular mechanisms of polymer chains associated with the stress overshoot phenomena upon exposure to the flow field.

Figure 4.2.5. The number N_{sec} of chains belonging to each angular section (normalized by the total number N of chains) and the corresponding intermolecular LJ shear stress $\sigma_{xy}^{\text{inter}}$ as a function of strain (Sec 1 is specified as $0° \le \theta \le 20°$, Sec 2 as $20° \le \theta \le 40°$, Sec 3 as $40° \le \theta \le 60°$, and Sec 9 as $160° \le \theta \le 180°$).

Figure 4.2.6. Vector field of the average angular velocity for clockwise (ω^+, black arrows) and counterclockwise (ω^-, red arrows) chain rotation at each orientation angle before stress overshoot.

Figure 4.2.7. The first normal stress difference N_1^{inter} of intermolecular LJ interaction and the mean-square chain end-to-end distance $\left\langle R_{\text{ete}}^2 \right\rangle$ for each angular section as a function of strain.

Figure 4.3.1. (Left) Transient behaviors of stress and chain structure. Relaxation behaviors of shear stress σ_{xy} (upper panel) and the first normal stress difference $N_1(\equiv \sigma_{xx} - \sigma_{yy})$ (bottom panel) for three different *Wi* numbers. The empty and filled symbols represent the corresponding (*xy* or *xx*–*yy*) component of the birefringence tensor $\mathbf{n}$ and the orientation tensor $\mathbf{S}$ of entanglement strands, respectively. (Right) Comparison of the transient behaviors of stress with those of the chain end-to-end distance $|\mathbf{R}|$ and orientation angle θ [the angle between the flow (*x*-)direction and the director which is the eigenvector corresponding to the largest eigenvalue of the order tensor based on the chain end-to-end vector].

Figure 4.3.2. Structural and orientational relaxation rates. Magnitude of structural relaxation rate $\frac{d|\tilde{\mathbf{R}}|}{dt}$ (upper panel) and orientational relaxation rate $\frac{d\tilde{\theta}}{dt}$ (bottom panel), evaluated by using an 8$^{\text{th}}$-order polynomial fit of $|\tilde{\mathbf{R}}|$ and $\tilde{\theta}$, for different *Wi* numbers.

Figure 4.3.3. Structural and orientational relaxation rates. Plots of the magnitudes of the structural relaxation rate $\frac{d|\mathbf{R}|}{dt}$ (solid lines) and the orientational relaxation rate $\frac{d\theta}{dt}$ (dashed lines) for each group of the steady-state chain end-to-end distance $|\mathbf{R}_{st-st}|$ relative to the equilibrium one $\langle|\mathbf{R}_{eq}|\rangle$ as a function of time for (Left) *Wi*=92.8 and (Right) *Wi*=371. Here, GR 1 is specified as

$\left\langle \left| \mathbf{R}_{eq} \right| \right\rangle < \left| \mathbf{R}_{st-st} \right| \le 2\left\langle \left| \mathbf{R}_{eq} \right| \right\rangle$ and GR 2 as $2\left\langle \left| \mathbf{R}_{eq} \right| \right\rangle < \left| \mathbf{R}_{st-st} \right|$. $\left\langle \left| \mathbf{R}_{eq} \right| \right\rangle$ = 89.52±14.14 Å for the simulated $C_{400}H_{802}$ PE melt. Note that each property is normalized (as indicated by the tilde symbol) as $\frac{\langle A \rangle - \langle A \rangle_{eq}}{\langle A \rangle_{st-st} - \langle A \rangle_{eq}}$ where $\langle A \rangle_{eq}$ and $\langle A \rangle_{st-st}$ are the equilibrium and steady-state values of a property A, respectively.

Figure 4.3.4. Relaxation of the correlation functions. Transient behavior of the correlation functions $C_{xy} = \langle u_x u_y \rangle - \langle u_x \rangle \langle u_y \rangle$ (solid lines) and $C_{xx-yy} = \langle u_x^2 \rangle - \langle u_y^2 \rangle$ (dashed lines) of the unit chain end-to-end vector **u** for different *Wi* numbers.

Figure 4.3.5. Structural evolution during relaxation. (Top) Transient behaviors of the probability distribution function (PDF) for the five representative mesoscopic chain configurations [end-kink (E-K), end-center-kink (E-C-K), coil, fold, stretch] computed from the brightness analysis upon cessation of steady shear at t = 0. (Bottom) Schematic description of the basic molecular characteristics of structural and orientational relaxation behaviors. Also shown are snapshots of a randomly selected chain at certain specific times during structural relaxation for *Wi* = 371.

Figure 4.3.6. Transient behaviors of stress and chain structure. Plots of (top) the shear stress σ_{xy} and (bottom) the first normal stress difference N_1 (solid lines) fitted by a simple exponential decay function $\tilde{\sigma}_{xy,xx-yy}(t) = \alpha e^{-t/\tau_1} + (1-\alpha)e^{-t/\tau_2}$ (dashed lines) for three different *Wi* numbers. τ_2 was fixed as equal to $0.7\tau_d$ for all *Wi* numbers. The threshold time regime is marked as red colored area around $t \simeq 2\tau_R$ where the structural and induced orientational relaxations become nearly complete.

Figure 4.3.7. Plot of $\frac{d \ln \langle R^2 \rangle}{dt} = -\frac{4k}{\xi} = -\frac{1}{\tau}$ vs. time for different *Wi* numbers.

Figure 4.3.8. Plots of the parameters α (upper panel) and $\tilde{\tau}_1 (= \tau_1 / \tau_d)$ (bottom panel) in a simple exponential decay function $\tilde{\sigma}(t) = \alpha e^{-t/\tau_1} + (1-\alpha)e^{-t/\tau_2}$ characterizing the relaxation behaviors of σ_{xy} and N_1 (Fig. 4.3.6) for different *Wi* numbers. Here τ_2 was fixed as equal to $0.7\tau_d$ for all *Wi* numbers. Additionally, the frictional coefficient ξ (the right y-axis in bottom panel) is calculated based on equation $\frac{\langle R^2 \rangle - \langle R^2 \rangle_{eq}}{\langle R^2 \rangle_{st-st} - \langle R^2 \rangle_{eq}} = \exp\left(-\frac{4k}{\xi} t \right) = \exp\left(-\frac{t}{\tau} \right)$ (Fig. 4.3.7).

List of Tables

Nomenclature

Symbol	Description	Unit
$\dot{\gamma}$, $\dot{\varepsilon}$	shear rate / elongational rate	
Wi	Weissenberg number	
L_x, L_y, L_z	Simulation box length x, y and z	Å (σ^2)
σ_f, σ_w, σ_{wf}, ε_f, ε_w, ε_{wf}	LJ interaction parameter of fluid (f), wall (w) and fluid-wall (wf)	σ, ε
d_s	Degree of slip	
$\langle Z_{es} \rangle$	The number of entanglements per chains	
$G_{\alpha\alpha,inf}$	$\alpha\alpha$-component of gyration tensors of interfacial chains	Å (σ^2)
y_{nadv}	y-component of center of mass of nonadsorbed segments	Å (σ)
$\langle R_g^2 \rangle$ $\langle R_{ete}^2 \rangle$	Mean squared radius of gyration / chain end-to-end distance	Å (σ^2)
H	Hamiltonian	
A, S	Free energy / entropy	
Ξ	Friction coefficient	
m, **a**, **v**	Mass, acceleration and velocity	g, m/s^2, m/s
p, **q**, t	Peculiar momentum vector, position vector and time	
τ_d, τ_d	Terminal relaxation time / Rouse time	
Δu	Velocity field	
Q, p_s, t_s	Nosé-Hoover thermostat variables	
n	Birefringence tensor	
L_{pp}	Primitive path	Å (σ)

Symbol	Description	Unit
Γ	Strain	
σ_{xy}, N_1	Shear stress / the 1st normal stress difference	
V_s, V	Slip velocity and upper wall velocity	
C_{xy} C_{xx-yy}	Correlation functions of the unit chain end-to-end vector **u**	

I. INTRODUCTION

The field of computer simulations has experienced significant advances and the rapid increase in computing power. These developments enable us to provide fundamental (from flowing polymeric systems to colloid, biomolecules or nanostructure materials undergoing mechanic or electric force field) by revealing the molecular origin of phenomena observed macroscopically and by suggesting a direct route between the microscopic information and macroscopic properties/phenomena (as a bridge). From DFT, all atom or coarse graining model, further to the continuum model such as the COMSOL or ABABUS, there are various ranges of scale of computer simulation (See Figure 1.1.1). In particular, molecular dynamics can measure the physical properties and phenomena directly at atomic or molecular level based on Newtonian and statistical mechanics. This allows us to study small systems that cannot be seen in the experiments. Moreover, it also gives comprehensive and systematic research in structural, thermodynamic and rheological properties of complex molecules at molecular level, via nonequilibrium molecular dynamics (NEMD) simulations.

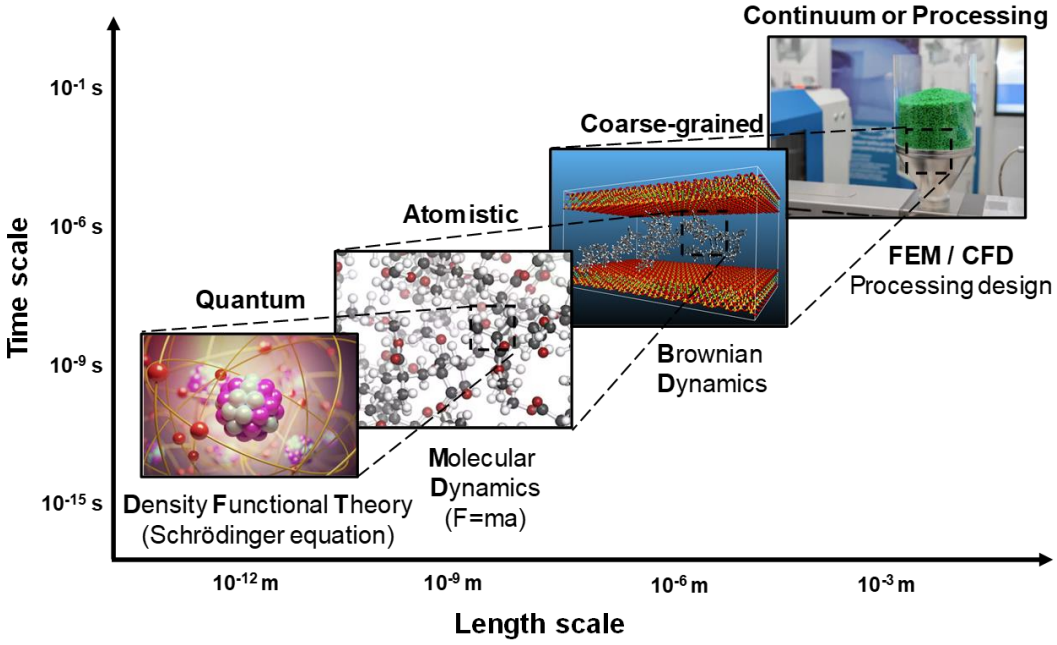

Figure 1.1.1. Computer simulation scale.

Motivated by advantages of the computer simulation, we attempted to elucidate fundamental molecular information of phenomena, where they generally occur in interfacial polymer systems, and also sheared polymeric melts systems undergoing various types of shear flow (e.g., startup-shear, steady shear, and cessation of steady shear flow).

In confined polymer system, structural or rheological properties of polymeric liquids are significantly

affected by interfacial slip on static wall. Confined or interfacial polymeric systems, commonly used in practical polymer processes, have attracted a lot of attention for many decades, owing to their versatile practical applications such as polymer films, polymer nanocomposites, biological membranes, and lubricants. It is well known that when a fluid is confined to a narrow geometry, its physical and chemical behaviors, e.g., solidlike behavior, high viscosity, and oscillatory solvation force are very different from those of the ordinary bulk fluid (See Figure 1.1.2).

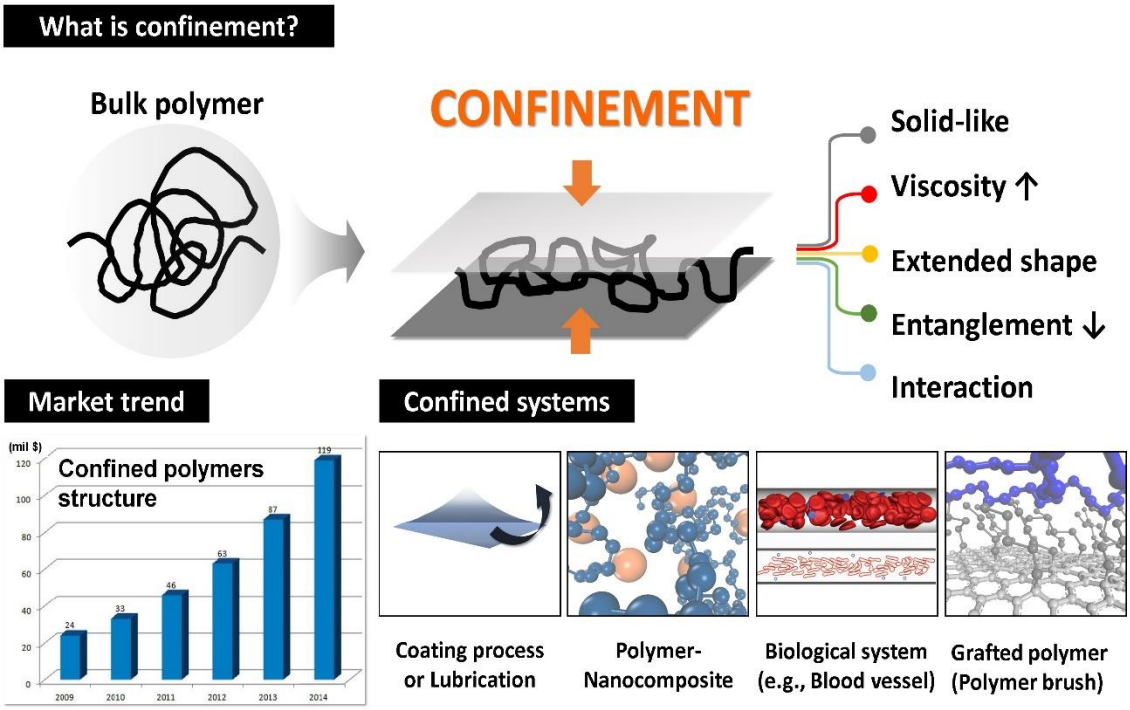

Figure 1.1.2. Basic information of confined polymeric systems.

In particular, the interfacial slip phenomena have been recognized as one of the most intriguing research topics since the pioneering work of Mooney because they deny the traditional no-slip boundary condition, the assumption that fluids at a fluid-wall interface move with the same velocity as that of the wall, which has been routinely applied to a variety of fluid dynamics problems. One of important interfacial phenomenon, melt instability exhibited by polymer extrudates are directly associated with the slip phenomena such as stick-slip mechanism shown by many studies. According to de Genne, universal features for general polymeric materials can be identified and be elucidated by scaling laws. Therefore, study on the scaling behavior of confined polymeric materials via systematic molecular simulation would greatly help to predetermine material properties in the range of our interest before performing any experiments. The present well-established theories of confinement were worked out by de Genne and Odijk who demonstrated a relation between chain extension (R) and confinement degree (H) (Figure 1.1.3).

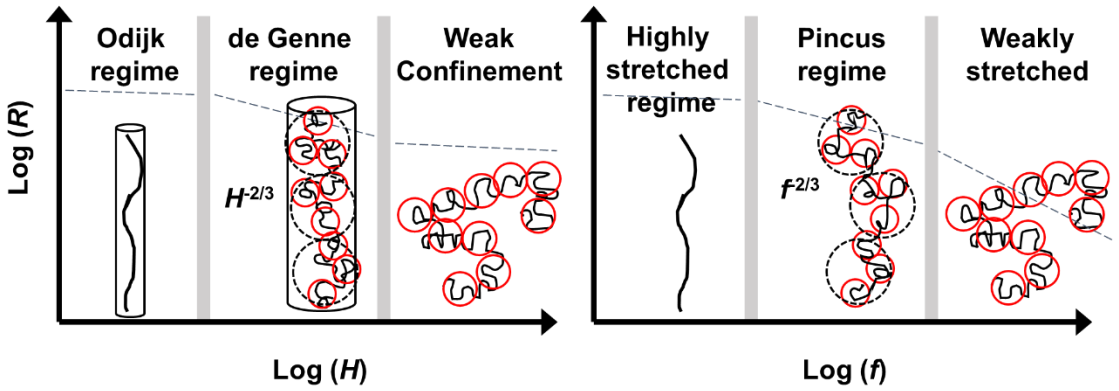

Figure 1.1.3. Scaling behavior of confined polymers.

The scaling of chain extension depending on applied force (f) was studied by Pincus. However, these works necessitate further exploration of the nature of such regimes, as the studied regimes have certain limitation based on several hypothetical assumptions (e.g., weak excluded volume effect). In other words, numerous scaling behaviors that have been reported to date often show controversial results one another or even in comparison with macroscopic properties. Therefore, our present knowledge of these interfacial phenomena at a microscopic level still remains controversial and incomplete. In-depth information of molecular mechanisms and dynamics behind such interfacial properties is essential to the development of our ability to predict and control intriguing behaviors of various confined systems. To our best knowledge, this work presents, for the first time, the detailed molecular mechanisms and dynamics underlying slip phenomena, which have yet to be established in interfacial polymer rheology. Elucidating the fundamental molecular characteristics behind the interfacial slip which is relevant to a variety of practical polymer processes, the present work would be beneficial for comprehending the general rheological characteristics and properties exhibited by interfacial polymeric systems. We consider the general features revealed in this study to be essentially intrinsic to any interfacial polymeric system, independent of various wall structures and polymer-wall interactions. Additionally, we extend to various polymers with complex molecular architectures and see structural and dynamic effects of polymer architecture on interfacial slip by directly tracking down the individual chain motion near the interface.

In the early stages of start-up shear at sufficient flow strengths, it is generally observed that stress increases with time and has maximum value, then eventually decreases to steady-state value (stress overshoot) in polymeric systems (Figure 1.1.4). Many experimental and theoretical studies have shown that the flow birefringence (a measure of the average bond-vector orientation) can properly describe both steady and transient stress behaviors for sheared polymeric liquids. According to the tube theory of entangled polymeric materials, the stress overshoot is closely related to the segmental (i.e., entanglement strand) orientation in the range of shear rates $\tau_d^{-1} < \dot{\gamma} < \tau_R^{-1}$, where τ_d and τ_R denote the

terminal relaxation time and the Rouse time, respectively, and segmental orientation determines responses of stress overshoot. Furthermore, for $\dot{\gamma} > \tau_R$, the global chain stretching makes a significant effect on the overshoot phenomenon for the normal stress as well as the shear stress. Various experimental and computational studies have supported these theoretical predictions; however, the detailed molecular mechanisms behind stress overshoot remain unclear. Based on these physical aspects, we thus carried out a detailed molecular analysis via NEMD to elucidate the intrinsic molecular characteristics and to provide fundamental answer to basic question behind the overshoot phenomena for entangled polymer systems experiencing shear flow.

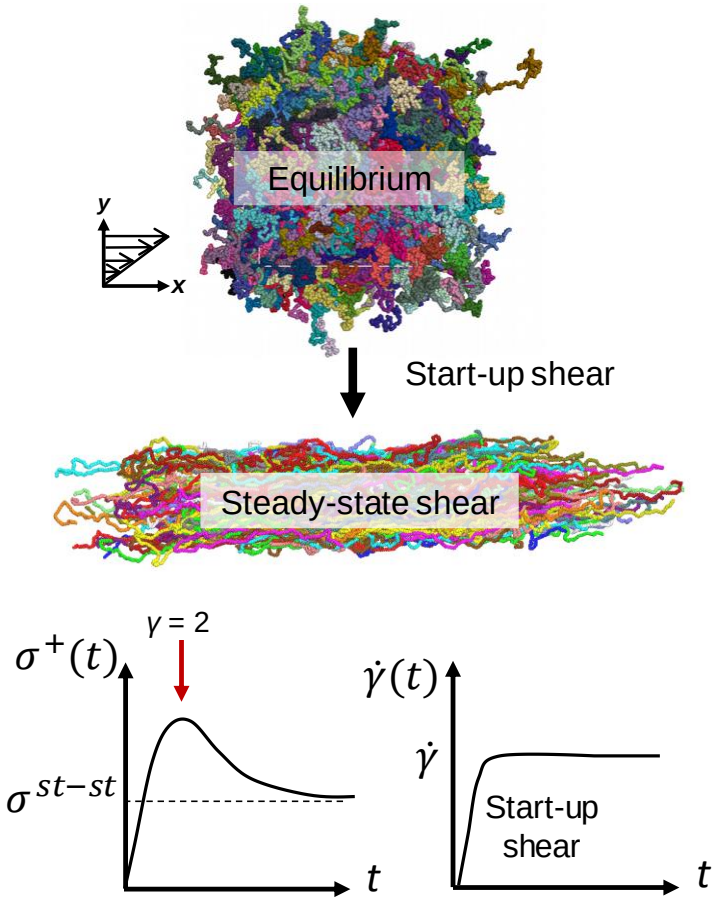

Figure 1.1.4. (Top) Atomistic description of systems undergoing start-up shear. (Bottom) Transient behavior of shear stress and shear rate as a function of time.

Unlike simple liquids that release applied stress almost instantaneously after the imposed external force field is turned off (Figure 1.1.5), polymeric liquids relieve stress gradually via complex structural and rheological transitions stemming from multiple characteristic time and length scales of various internal microstructures. Stress relaxation behaviors have been most widely applied in the field of polymer rheology for characterization of material properties in practice and for theoretical development of general constitutive models. However, detailed microscopic structural and dynamical processes

underlying the stress relaxation of polymer systems remain unknown. In this study, we aim to elucidate the basic molecular characteristics of the stress relaxation process occurring in polymer systems upon cessation of steady shear flow. An attempt is made to explain, based on the molecular features, the physical origins for some well-known experimental observations related to the stress relaxation phenomena of polymeric liquids.

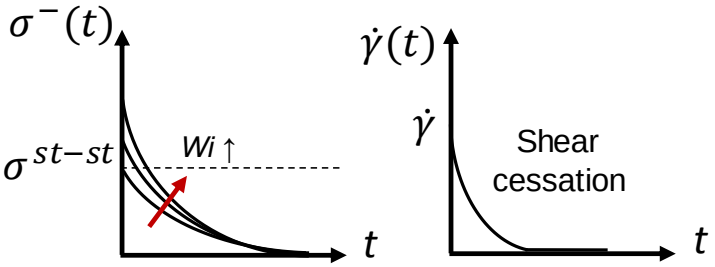

Figure 1.1.5. Transient behavior of shear stress and shear rate as a function of time upon cessation of steady shear.

II. BACKGROUND

2.1 Polymer physics

This chapter concentrates on the dynamics of polymers in the liquid state. Polymer liquid [which has its internal microstructure (i.e., entropy)] generally shows viscous and elastic characteristics (i.e., viscoelasticity), thus inducing its distinctive dynamical properties. Based on the statistical mechanics, polymer physics mostly aims to investigate the scaling behavior of polymers in the view of correlation length scale. Here, there are two main polymer models according to entanglements: Rouse (unentangled) and reptation (entangled) models.[1] As mentioned, polymer regarded as macromolecules, possesses internal microstructure, thus influenced by surrounding chain interaction in the range of sufficiently large length scale. This constraint, termed an entanglement can involve overall chain dynamics and statics, eventually giving rise to different behaviors according to degree of entanglements. With this aspect, unentangled and entangled models will be discussed in detail.

2.1.1 Unentangled polymer dynamics

Unentangled polymer model, called Rouse model (also known as bead-entropic spring model) describes dynamics by dividing polymer chains with *N* beads and *N*-1 springs (size *b*) based on Gaussian spring (Gaussian spring constant $k = \frac{3k_BT}{b^2}$, where k_B and b denote Boltzmann constant and Kuhn length) as depicted in Fig. 2.1.1. Ignoring an energetic effect in polymer, entropic effect (associated with chain length) is only considered, thus this leads a following equation:

$$A(\vec{r}) \approx -TS(\vec{r}) = -k_BT \ln \Psi(\vec{r}) = \frac{3k_BT}{2b^2} r^2 \tag{2.1.1}$$

where $A(\vec{r})$ and $S(\vec{r})$ represent free energy and entropy of the chains with bead vector $\vec{r}$ respectively, and $\Psi(\vec{r})$ denotes probability function of a chains with $\vec{r}$. Then spring force can be derived as follows.

$$F(\vec{r}) = -\frac{3k_BT}{b^2}\vec{r}, (k = \frac{3k_BT}{b^2}) \tag{2.1.2}$$

The equations of motions of Rouse model are eventually described by Langevin equation[2] as

$$\xi \frac{d\vec{r_i}}{dt} = -\frac{dU^{spring}}{d\vec{r_i}} + \vec{f_i} \tag{2.1.3}$$

representing ξ denotes friction coefficient U^{spring} and $\vec{f_i}$ are interaction potential and Brownian force, respectively. This equation can be approximately written as follows:

$$\xi \frac{\partial \vec{r_i}}{\partial t} = -\frac{\partial^2 \vec{r_i}}{\partial i^2} + \vec{f_i} \tag{2.1.4}$$

Note that Rouse model neglects excluded volume effect and hydrodynamic interaction; therefore it effectively elucidates dynamics of unentangled polymer melts. Additionally, the chain diffuses its length scale, called Rouse time τ_R:

$$\tau_R = \frac{\xi N^2 b^2}{3\pi^2 k_BT} \tag{2.1.5}$$

This indicates the chain is diffusive on time longer than Rouse time, whereas the chain has modes on time shorter than the Rouse time. From the Einstein relation, diffusion coefficient *D* of the Rouse chain is also written as

$$D = \frac{k_BT}{N\xi} \tag{2.1.6}$$

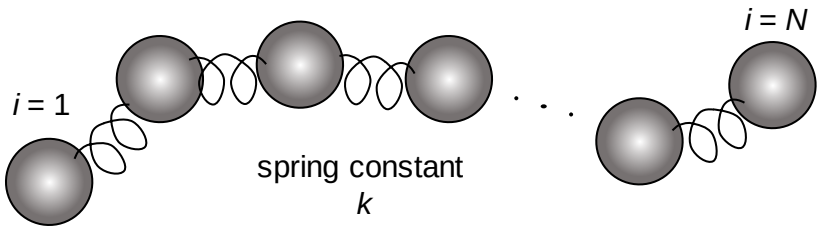

Figure 2.1.1. Schematic of a Rouse chain with *N* beads and *N*-1 springs (with spring constant *k*).

2.1.2 Entangled polymer dynamics

The topological constraints (entanglements) exhibited by surrounding chain interaction restrict chain motions, thus chains show biased motion in a tube-like region (see Fig. 2.1.2). The chains can freely move along their contour of the tube (called primitive path l_{pp}) due to hindered movement in direction perpendicular to the primitive path, termed tube diameter a. In tube (reptation) model, it describes entangled chain dynamics based on Rouse chain, in conjunction with constraints imposed by neighboring chains. Thus, here it is assumed that chains consist of N segments with length b and friction coefficient ξ.

In the short time scale, the chain shows small perturbation along its contour length. However, on a longer time scale, primitive path would change, generating or destroying original primitive path. This longest relation time, reptation time τ_d is

$$\tau_d = \frac{1}{\pi^2}\frac{\xi N^3 b^4}{k_B T a^2} \tag{2.1.7}$$

Importantly, τ_d is proportional to N^3, compared with τ_R (which is proportional to N^2), indicating dominant effect of topological constraints in entangled polymeric systems.

Additionally, primitive chains previously mentioned are regarded as inextensible contour length, without considering mobile tube (i.e., constraint release)[3] and contour length fluctuation[4]. However, in reality, the length of primitive fluctuates with time, also whole tube can move due to thermal Brownian effect, eventually leading to $\tau_d \sim N^{3.4}$ rather than N^3 obtained from assumption of constant contour length.

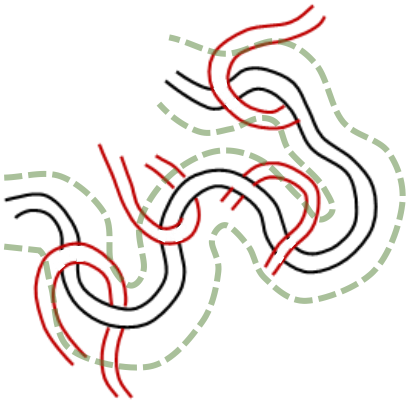

Figure 2.1.2. Description of a tube-like region (represented by green dash) of a reference chain (black) resulted from neighboring chains (red) which restrict a reference chain movement.

2.2 Polymer rheology

2.2.1 Introduction

Rheology[5] is the study of the deformation or flow of materials. It aims to demonstrate the flow behaviors of complex fluids (e.g., polymers, biosystems, suspensions, emulsions or compounds etc.) under the imposed flow field. The crucial goal of the rheology is to establish the relationship between the stress on material and deformation by measurements. Particularly, polymer-based flow behavior is to help understand the structure-property relationship. Because most polymeric materials do not follow the conventional Newtonian constitutive equation, the stress is highly complicated function of material properties. Thus, it is challenging and important in the field of rheology to constitutive equations for non-Newtonian fluids. To achieve this goal, many experiments have been carried out using various flow types. The resulting stress responses on the flow would be functions of time, strain or other parameters, which are dependent on fluid characteristics. Here, the functions that characterize the rheological (flow) behaviors of fluid is called material functions (e.g., stress, viscosity, modulus etc.). This chapter thus focuses on what kinds of standard flow type are and how material function (stress) become different under corresponding flow fields.

2.2.2 Standard flows: shear and elongational flow

To describe flow behavior, stresses generated by the flowing fluid should be measured when subjected to a deformation. Otherwise, we could measure the velocity or deformation resulted from the imposed stress on a fluid. Either of approaches can give us information of flow behavior. Two main flow type described here is shear and elongation.

Shear flow is the most general flow type in rheology. Velocity under shear flow is the only function of *y*-direction. Thus, the velocity field Δu for simple shear flow is defined in terms of Cartesian coordinates as follows.

$$\Delta u = \begin{pmatrix} \dot{\gamma} y \\ 0 \\ 0 \end{pmatrix} \tag{2.2.1}$$

where $\dot{\gamma}$ is shear rate defined as $\frac{\partial v_x}{\partial y}$. Therefore, in Cartesian coordinates, *x*-direction represents flow direction, *y*-direction is flow gradient direction, and *z*-direction is called the neutral direction. This

flow is produced when the fluid undergoes constant shear rate. Note that the stress tensor σ predicted by the Newtonian constitutive equation can be written as

$$\sigma = \eta\dot{\gamma} = \eta\frac{\partial v_x}{\partial y} \tag{2.2.2}$$

where η denotes viscosity. In addition, there are time-dependent shear flow types as well. Steady and unsteady shear flow types are compared and summarized in Figure 2.2.1.

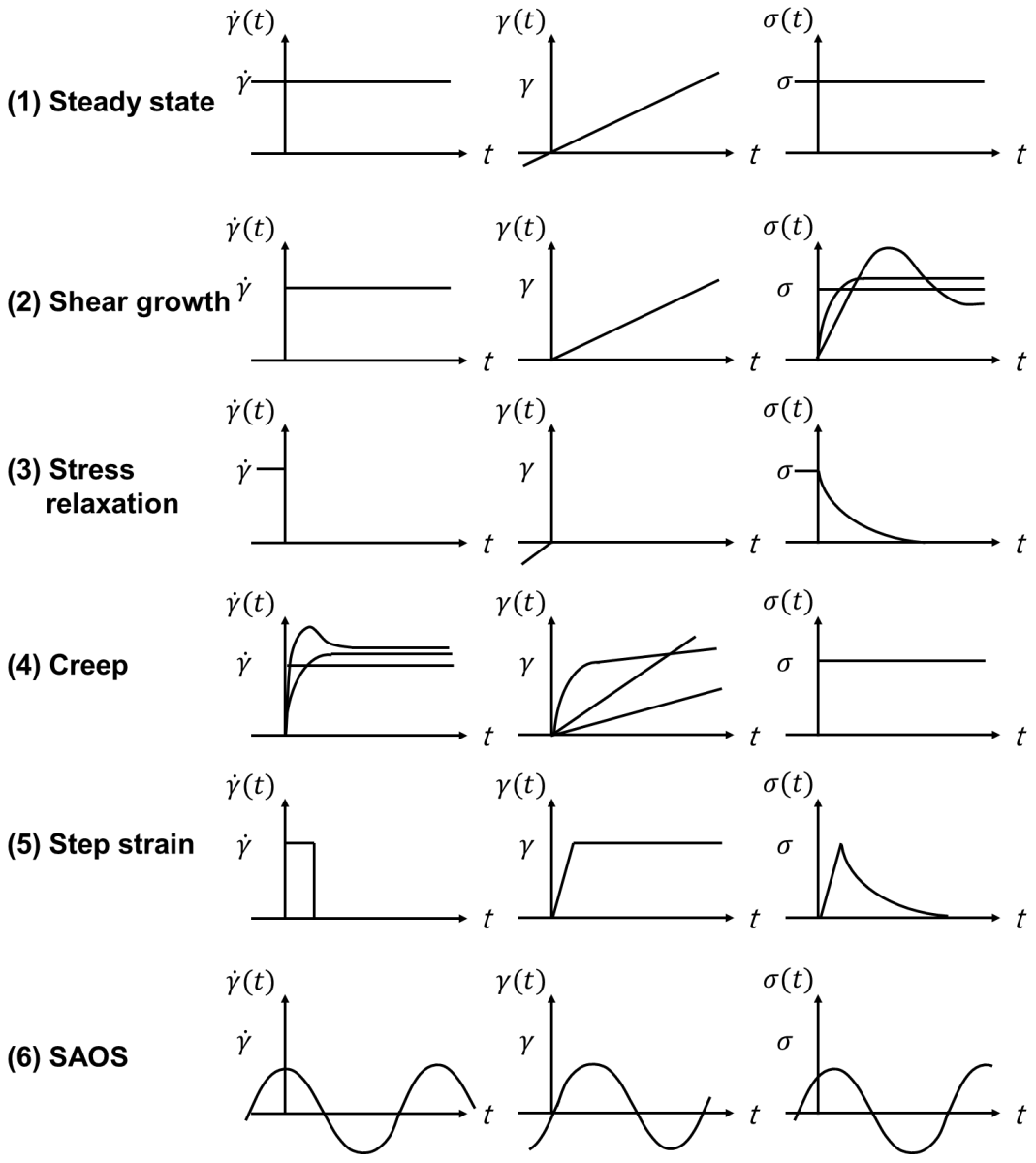

Figure 2.2.1. Summary of shear rate $\dot{\gamma}$, strain γ, and shear stress σ under steady and unsteady shear flow type.

Elongational flow, which is shear-free flow, is one including zero off-diagonal components in velocity field. The called uniaxial elongational (extensional) flow in Cartesian coordinates is described by the following velocity field:

$$\Delta u = \begin{pmatrix} \frac{-\dot{\varepsilon}}{2} x \\ \frac{-\dot{\varepsilon}}{2} y \\ \dot{\varepsilon} z \end{pmatrix} \tag{2.2.3}$$

where $\dot{\varepsilon}$ is (always positive) elongation rate. Therefore, a fluid exposed to uniaxial elongational flow would undergo both stretch in *z*-direction and contraction in *x*- and *y*-direction. Beginning with the Newtonian constitutive equation, we can obtain the stress tensor for a Newtonian fluid in steady elongational flow:

$$\sigma = \eta\dot{\gamma} = \eta \begin{pmatrix} -\dot{\varepsilon} & 0 & 0 \\ 0 & -\dot{\varepsilon} & 0 \\ 0 & 0 & 2\dot{\varepsilon} \end{pmatrix} \tag{2.2.4}$$

The other types of elongational flow is biaxial and planar elongational flows. Former has the same velocity profile form with uniaxial elongational flow except negative elongational rates, and later has no deformation in the *y*-direction. Velocity field in biaxial elongational flow in Cartesian coordinates is represented as

$$\Delta u = \begin{pmatrix} \frac{-\dot{\varepsilon}}{2} x \\ \frac{-\dot{\varepsilon}}{2} y \\ \dot{\varepsilon} z \end{pmatrix}, \dot{\varepsilon} < 0 \tag{2.2.5}$$

And planar elongational flow in Cartesian coordinates is defined by the following velocity profile:

$$\Delta u = \begin{pmatrix} -\dot{\varepsilon} x \\ 0 \\ \dot{\varepsilon} z \end{pmatrix} \tag{2.2.6}$$

III.COMPUTATIONAL

3.1 Nonequilibrium molecular dynamics simulation

3.1.1 Steady shear flow

Computer simulation has been numerous developed in computational method and algorithm, and currently it has become essential parts in many research fields, along with theories and experiments.

Molecular dynamics (MD) simulation, the most powerful computational method, computes the positions and velocities of individual particles by solving their equations of motion as a function of time, based on classical Newtonian equation:

$$\mathbf{F} = m\mathbf{a} = m\frac{d\mathbf{v}}{dt} \tag{3.1.1}$$

where **F** is the force acting on the particle, **a** is acceleration of particle, m is its mass, **v** is its velocity, and t is time. Thus, it is possible to express the Hamiltonian of a system followed by

$$H(\mathbf{p},\mathbf{q}) = \sum_{i}^{N}\frac{\mathbf{p}_i \cdot \mathbf{p}_i}{2m_i} + U(\mathbf{q}_1,...,\mathbf{q}_N) \tag{3.1.2}$$

where $\mathbf{p}_i$ and $\mathbf{q}_i$ denote the momentum and coordinate of particle i, respectively, N the number of particles, and U the potential energy of system. The Hamiltonian's equations of motion are then expressed as

$$\dot{\mathbf{q}}_i = \frac{\partial H}{\partial \mathbf{p}_i} = \frac{\mathbf{p}_i}{m_i} \tag{3.1.3}$$

$$\dot{\mathbf{p}}_i = -\frac{\partial H}{\partial \mathbf{q}_i} = \mathbf{F}_i \tag{3.1.4}$$

The atomistic NEMD simulations were executed with the *p*-SLLOD algorithm proposed by Baig *et al.*[6,7] implemented with the Nosé-Hoover thermostat[8,9] for external velocity gradient field $\nabla\mathbf{u}$. The corresponding canonical equations of motion are written as

$$\begin{aligned}\dot{\mathbf{q}}_i &= \frac{\mathbf{p}_i}{m_i} + \mathbf{q}_i \cdot \nabla \mathbf{u} \\ \dot{\mathbf{p}}_i &= \mathbf{F}_i(\mathbf{q}) - \mathbf{p}_i \cdot \nabla \mathbf{u} - m_i \mathbf{q}_i \cdot \nabla \mathbf{u} \cdot \nabla \mathbf{u} - \frac{p_s}{Q}\mathbf{p}_i \\ \dot{s} &= \frac{sp_s}{Q} \\ \dot{p}_s &= F_s(\mathbf{p}_i)\end{aligned} \tag{3.1.5}$$

where s and p_s are coordinate- and momentum-like variables, respectively, of the Nosé-Hoover thermostat. $Q=DNk_BT\tau^2$ is the thermostat mass parameter where D and τ are the dimensionality and relaxation time parameter, respectively. This p-SLLOD algorithm has been proved to show a rigorously canonical structure with satisfying thermodynamics and Newtonian mechanics.

Also, we utilized the reversible reference system propagator algorithm (r-RESPA)[10] to numerically integrate the evolution equations. The time propagator $\mathbf{G}(\Delta t)$ for each atom can be derived as follows:

$$\begin{aligned}\mathbf{G}(\Delta t) = &\exp[\frac{\Delta t}{2}F_s\frac{\partial}{\partial p_s}]\exp[\frac{\Delta t}{4}\mathbf{f}(\mathbf{r}_i)\frac{\partial}{\partial \mathbf{p}_i}]\exp[-\frac{\Delta t}{2}\frac{p_s}{Q}\mathbf{p}_i\cdot\frac{\partial}{\partial \mathbf{p}_i}] \\ &\times\exp[\frac{\Delta t}{4}\mathbf{f}(\mathbf{r}_i)\frac{\partial}{\partial \mathbf{p}_i}]\exp[-\frac{\Delta t}{2}m_i\mathbf{r}_i\cdot(\nabla u)_{input}\cdot(\nabla u)_{input}\frac{\partial}{\partial \mathbf{p}_i}] \\ &\times\exp[-\frac{\Delta t}{2}\mathbf{p}_i\cdot(\nabla u)_{input}\frac{\partial}{\partial \mathbf{p}_i}]\exp[\frac{\Delta t}{2}\frac{sp_s}{Q}\frac{\partial}{\partial s}]\exp[\frac{\Delta t}{2}\mathbf{r}_i\cdot(\nabla u)_{input}\frac{\partial}{\partial \mathbf{r}_i}] \\ &\times\exp[i\mathbf{L}_R\Delta t]\exp[\frac{\Delta t}{2}\mathbf{r}_i\cdot(\nabla u)_{input}\frac{\partial}{\partial \mathbf{r}_i}]\exp[\frac{\Delta t}{2}\frac{sp_s}{Q}\frac{\partial}{\partial s}] \\ &\times\exp[-\frac{\Delta t}{2}\mathbf{p}_i\cdot(\nabla u)_{input}\frac{\partial}{\partial \mathbf{p}_i}]\exp[-\frac{\Delta t}{2}m_i\mathbf{r}_i\cdot(\nabla u)_{input}\cdot(\nabla u)_{input}\frac{\partial}{\partial \mathbf{p}_i}] \\ &\times\exp[\frac{\Delta t}{4}\mathbf{f}(\mathbf{r}_i)\frac{\partial}{\partial \mathbf{p}_i}]\exp[-\frac{\Delta t}{2}\frac{p_s}{Q}\mathbf{p}_i\cdot\frac{\partial}{\partial \mathbf{p}_i}]\exp[\frac{\Delta t}{4}\mathbf{f}(\mathbf{r}_i)\frac{\partial}{\partial \mathbf{p}_i}]\exp[\frac{\Delta t}{2}F_s\frac{\partial}{\partial p_s}]\end{aligned} \tag{3.1.6}$$

The Liouville operator $\mathbf{L}_R$ of the reference system is defined as

$$i\mathbf{L}_R = \frac{\mathbf{p}_i}{m_i}\frac{\partial}{\partial \mathbf{r}_i} + \mathbf{F}_R(\mathbf{r}_i)\frac{\partial}{\partial \mathbf{p}_i} \tag{3.1.7}$$

3.1.2 Unsteady shear flow: start-up shear and cessation of steady shear flow

Note that in start-up shear (i.e., $\nabla_y \mathbf{u}_x = \dot{\gamma}$) or cessation of steady shear flow (i.e., $\nabla\mathbf{u} = \mathbf{0}$), streaming velocity $\mathbf{U}(\mathbf{q}_i)$ along the velocity gradient direction gradually develops or diminishes as a function of time, eventually reaching the steady-state velocity of corresponding imposed strain rate or

equilibrium state, respectively. The streaming velocity $\mathbf{U}(\mathbf{q}_i)$ at atomic position $\mathbf{q}_i$ was computed based on a 5th-order polynomial fit in every MD step throughout the system. The velocity gradient tensor for simple shear flow is expressed as

$$\nabla\mathbf{u} = \begin{pmatrix} 0 & 0 & 0 \\ \dot{\gamma} & 0 & 0 \\ 0 & 0 & 0 \end{pmatrix} \tag{3.1.8}$$

for planar Couette flow with shear rate $\dot{\gamma}$. The applied shear rate is expressed in reduced unit $\dot{\gamma}^* = \dot{\gamma}\, t_{\mathrm{ref}}$ where dimensionless time $t_{\mathrm{ref}} = (\sigma^2 m/\varepsilon)^{1/2}$. The real peculiar momentum $\mathbf{p}_i^{\mathrm{real}}$ of each atom was then calculated by subtracting the streaming velocity at its position from its laboratory momentum $\mathbf{p}_i' = \mathbf{p}_i + m_i\mathbf{q}_i \cdot \nabla\mathbf{u}$: $\mathbf{p}_i^{\mathrm{real}} = \mathbf{p}_i' - m_i\mathbf{U}(\mathbf{q}_i)$. Then this finally gives corresponding equations of motion:

$$\begin{aligned}
\dot{\mathbf{q}}_i &= \frac{\mathbf{p}_i}{m_i} + \dot{\mathbf{q}}_i \cdot \nabla\mathbf{u} \\
\dot{\mathbf{p}}_i &= \mathbf{F}_i(\mathbf{q}) - \mathbf{p}_i \cdot \nabla\mathbf{u} - m_i\mathbf{q}_i \cdot \nabla\mathbf{u} \cdot \nabla\mathbf{u} - \frac{p_s}{Q}\mathbf{p}_i - \frac{p_s}{Q}(m_i\mathbf{q}_i \cdot \nabla\mathbf{u} - m_i\mathbf{U}(\mathbf{q}_i)) \\
\dot{s} &= \frac{p_s}{Q} \\
\dot{p}_s &= F_s(\mathbf{p}_i)
\end{aligned} \tag{3.1.9}$$

3.2 Simulation model and system details

The well-known (Siepmann-Karaborni-Smit) SKS[11] and Transferable Potentials for Phase Equilibria (TraPPE)[12] united-atom potential model were adopted for systems, except for that the rigid bond adopted in the original model was replaced by a flexible one with a harmonic potential. In the SKS and TraPPE models, nonbonded intermolecular and intramolecular interactions between atomic units were represented by the 6-12 Lennard-Jones (LJ) potential:

$$U_{LJ}(r) = 4\varepsilon_{ij}\left[\left(\frac{\sigma_{ij}}{r}\right)^{12} - \left(\frac{\sigma_{ij}}{r}\right)^{6}\right] \tag{3.2.1}$$

where $\varepsilon_{ij}=(\varepsilon_i\varepsilon_j)^{1/2}$ and $\sigma_{ij}=(\sigma_i+\sigma_j)/2$ were defined by the standard Lorentz-Berthelot mixing rules between atomistic units i and j. The LJ parameters in the SKS model were put equal to ε/k_B = 47 K and σ=3.93 Å for the CH_2 units, and equal to ε/k_B = 114 K and σ=3.93 Å for the CH_3 units, where k_B denotes the Boltzmann constant. And the size parameters in the TraPPE model σ_{CH}, σ_{CH2}, and σ_{CH3} were set equal to 4.68 Å, 3.95 Å, and 3.75 Å, respectively, and the energy parameters ε_{CH}/k_B, ε_{CH2}/k_B, and ε_{CH3}/k_B, equal to 10 K, 46 K, and 98 K, respectively. A cut-off distance equal to 2.5 σ_{ij} was utilized in the simulations. The intramolecular LJ interaction was only active between atoms that are farther apart than three bonds along the chain. The bond-stretching, bond-bending, and bond-torsional interactions are described by the following expressions:

$$U_{stretching}(l) = \frac{k_{str}}{2}(l - l_{eq})^2 \tag{3.2.2}$$

$$U_{bending}(\theta) = \frac{k_{ben}}{2}(\theta - \theta_{eq})^2 \tag{3.2.3}$$

and

$$U_{torsional}(\phi) = \sum_{m=0}^{3} a_m \cos^m \phi \tag{3.2.4}$$

where the bond-stretching constant k_{str}/k_B = 452,900 K/Å^2, the equilibrium bond length l_{eq} = 1.54 Å, the bond-bending constant k_{ben}/k_B = 62,500 K/ rad^2, the bond-torsional constants a_0/k_B = 1010 K, a_1/k_B = 2019 K, a_2/k_B = 136.4 K and a_3/k_B = – 3165 K with the equilibrium bond angle θ_{eq} = 114° for the SKS model. In the TraPPE model, the equilibrium bending angle θ_{eq} = 114° for CH_x-CH_2-CH_y (with x and y equal to 2 or 3), θ_{eq} = 112° for CH_x-CH-CH_y, and θ_{eq} = 109.47° for CH_x-C-CH_y. The bond-torsional parameters are such that (a) a_0 = 2.0071, a_1 = 4.0122, a_2 = 0.27105, a_3 = −6.2895 (kcal/mol) for CH_x-CH_2-CH_2-CH_y, (b) a_0 = 0.78542, a_1 = 1.7787, a_2 = 0.44454, a_3 = −3.5076 (kcal/mol) for CH_x-CH_2-CH-CH_y, and (c) a_0 = 0.91670, a_1 = 2.7503, a_2 = 0, a_3 = −3.6665 (kcal/mol) for CH_x-CH_2-C-CH_y [note that

here $\phi = 0$ represents the (most stable) *trans*-conformation, whereas it refers to the *cis*-conformation].

We have carried out direct atomistic NEMD simulations of various entangled linear polyethylene (PE) melts with complicated chain architectures under unsteady and steady shear in a wide range of flow strengths, corresponding to the Weissenberg number *Wi* (defined as the product of the terminal relaxation time τ_d of the system and the imposed strain rate $\dot{\gamma}$). The NEMD simulations were executed with the well-known *p*-SLLOD algorithm[6,7], implemented by a Nosé–Hoover thermostat[8,9] and the standard Lees–Edwards sliding-brick boundary conditions[13] using the reversible reference system propagator algorithm (*r*-RESPA)[10] (see Table 3.2.1 for details of the systems).

Table 3.2.1 Detailed information of the systems simulated

System	Polymer	UA model	Wall type	Density	Pressure	Temperature	Flow type	Flow strength	Relaxation time
				ρ (g/cm^3)	P (atm)	T (K)	$\dot{\gamma}$	$Wi \equiv \tau_d \dot{\gamma}$	τ_d (ns)
Bulk L400	Linear $C_{400}H_{802}$	SKS	·	0.7640	1	450	Startup-shear/ Cessation of steady shear	$3.71 \le Wi \le 928$ $18.6 \le Wi \le 928$	218
Confined L30 Confined L128 Confined L178 Confined L400	Linear $C_{30}H_{62}$ $C_{128}H_{258}$ $C_{178}H_{358}$ $C_{400}H_{802}$	SKS TraPPE SKS SKS	Simple cubic	0.795 0.7684 0.789 0.769	1	350 450 450 450	Steady shear	$0.17 \le Wi \le 460$ $1.76 \le Wi \le 4410$ $0.68 \le Wi \le 5600$ $45 \le Wi \le 44000$	2.1 20.7 26.7 525
Confined SCB178	Short-chain branched $C_{178}H_{358}$	TraPPE	Simple cubic	0.7745	1	450	Steady shear	$6.04 \le Wi \le 7750$	35.5
Confined R128 Confined R400	Ring $C_{128}H_{256}$ $C_{400}H_{800}$	TraPPE	Simple cubic	0.7700 0.7390	1	450	Steady shear	$1.09 \le Wi \le 544$ $0.91 \le Wi \le 2282$	2.55 10.9

IV. RESULTS AND DISCUSSION

4.1 Confined polymer melts under steady-shear flow

Confined or interfacial polymeric systems, commonly used in practical polymer processes, have been largely investigated, due to resolving interfacial phenomena occurring in polymer films, adhesion, nanocomposites or lubricants. However, despite numerous efforts, its intrinsic molecular characteristics is still unclear. Interfacial slip, especially, one of significant interfacial phenomena, has been studied for several decades, but there are lots of questions on molecular origin of the phenomenon in spite of its significance.

In this regard, we conducted a comprehensive and thorough analysis on the interfacial polymer chains via direct atomistic NEMD simulations of PE melts with different chain architecture (linear, short-chain branched, ring) under steady shear in a wide range of flow strength. Here the intrinsic molecular characteristics of the slip phenomena of polymer melts is introduced. Our results identify three distinctive characteristic regimes with regard to the degree of slip (d_s), and reveal the underlying molecular mechanisms for each regime. Also we mainly focus on comparison between each melts system of different chain structure on interfacial dynamics.

4.1.1 Interfacial slip

The no-slip boundary condition (which is zero velocity on static wall) had been considered in conventional fluid mechanics, but most realistic systems do not follow this condition, as reported in previous studies. Although the occurrence of slip phenomena is well-accepted, slip is a on complicated function of chain length, chain architecture, wall structure, wettability, etc., thus it has been required to investigate for several decades.

When the fluid has nonzero velocity V_s on a static wall, the slip length L_s can be estimated by extrapolation of velocity profile near the bottom wall, as depicted in Figure 4.1.1. The nonzero finite velocity is called the slip velocity. The slip velocity V_s and slip length L_s have the following relation according to the Navier model.

$$V_s = L_s \dot{\gamma}_{real} \tag{4.1.1}$$

where $\dot{\gamma}_{real}$ is the real shear rate, as computed from the actual velocity profile.

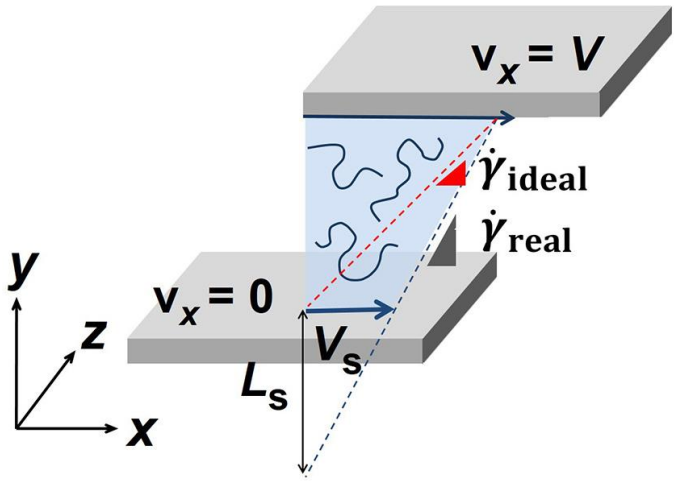

Figure 4.1.1 Schematic drawing of a steady-state velocity profile under simple shear flow with the upper wall moving with velocity, V and the bottom wall being fixed.

4.1.2 Linear polymer melts

The atomistic *NVT* NEMD simulations of the linear PE melts[33] under shear flow were executed with the *p*-SLLOD algorithm,[6,7] implemented with the Nosé-Hoover thermostat[8,9] using the *r*-RESPA[10] in a wide range of shear rates $\dot{\gamma}$, corresponding to Weissenberg numbers $0.17 \le Wi \equiv \lambda\dot{\gamma} \le 460$ with λ=2.09 ns for the $C_{30}H_{62}$, $0.68 \le Wi \equiv \lambda\dot{\gamma} \le 5600$ with λ=26.69 ns for the $C_{178}H_{358}$ system, and $220 \le Wi \equiv \lambda\dot{\gamma} \le 44000$ with λ=525 ns for $C_{400}H_{802}$ system. The NEMD simulations were performed at constant temperature of T = 350 K and density of ρ = 0.795 g/cm^3 for $C_{30}H_{62}$, T = 450 K and ρ = 0.789 g/cm^3 for $C_{178}H_{358}$, and T = 450 K and ρ = 0.769 g/cm^3 for $C_{400}H_{802}$ (corresponding to the pressure P = 1atm in each confined system).

In this work, we have identified three distinctive characteristic regimes in terms of the degree of slip d_s (Fig. 4.1.2). Here, the degree of slip is defined as follows: $d_s = 1 - \frac{\dot{\gamma}_{real}}{\dot{\gamma}_{ideal}} = \left(\frac{V}{H} - \frac{V - V_s}{H} \right) / \frac{V}{H} = \frac{V_s}{V}$ where H is the length of the simulation box in the velocity gradient (y-)direction. $\dot{\gamma}_{ideal} = V/H$ represents the ideal (nominal) shear rate assuming no-slip boundary condition and $\dot{\gamma}_{real} = (V - V_s)/H$ denotes the real shear rate resulting from slip. d_s together with the streaming velocity was directly evaluated by using a 5^{th}-order polynomial fit in every MD step throughout the whole confined system and by averaging over a sufficiently long system trajectory (see ref 33 and the Supporting Information therein for additional details). And each characteristic regime is represented by vertical line for each melts system. In the first (weak flow) regime, interfacial polymer chains undergo the z-to-x rotation in the vorticity plane because of the imposed shear flow (x-direction). This effectively diminishes the wall friction against chain movement along the flow direction, giving rise to an increase of d_s. In the second (intermediate flow) regime, the flow strength becomes comparable to the wall friction, thus resulting in the repetitive chain detachment-attachment (out-of-plane wagging). This leads to a plateau value of d_s for unentangled melts. For entangled melts, however, d_s rather decreases due to a disentanglement mechanism between interfacial and bulk chains, by more aligned bulk chains with increasing flow strength. As the strong flow regime, d_s increases again for all systems. This regime is mainly governed by chaotic (irregular) chain rotation and tumbling mechanisms via strong molecular collisions between interfacial chains and the wall. In accordance with these molecular dynamics, the interfacial residence time is found to significantly decrease in the third regime while it is nearly invariable in the first and second regimes. Thus, interfacial chains are observed to intermix intensely with bulk chains. From a molecular point of view, the second and the third regimes are thus characterized as dynamically stable and unstable (chaotic) flow ranges in interfacial molecular mechanisms and dynamics.

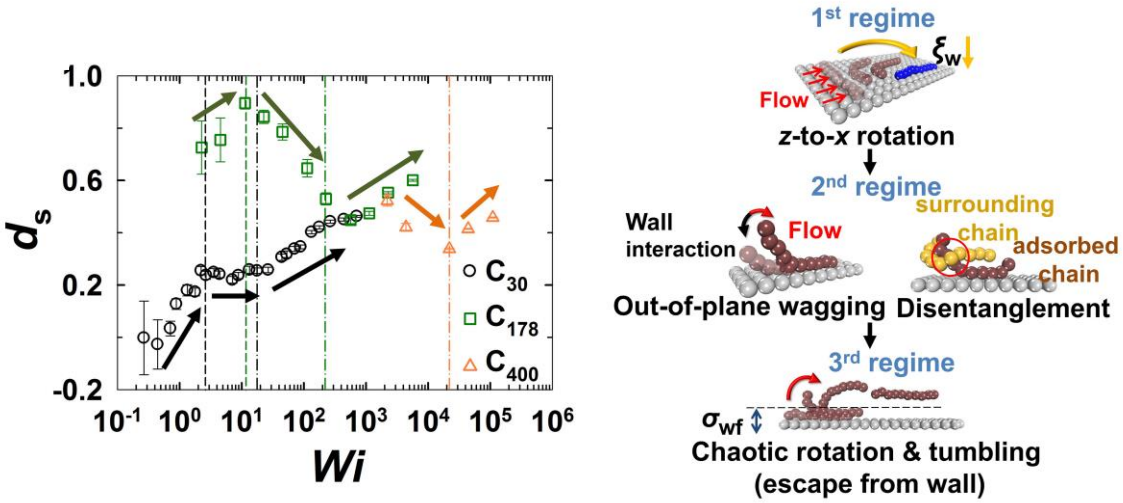

Figure 4.1.2 Three regimes of degree of slip. (Left) Variation of the degree of slip (d_s) with shear rate for the simulated $C_{30}H_{62}$, $C_{178}H_{358}$, and $C_{400}H_{802}$ polyethylene melts with the polymer-wall LJ interaction energy parameter ε_{wf}=4.47 ε (ε/k_B=47 K). The three characteristic regimes are separately represented by vertical lines for each melt. (Right) Schematic description of the main molecular mechanisms and dynamics directly related with the interfacial slip for each of the three regimes.

4.1.3 Short-chain branched polymer melts

To adequately demonstrate a detailed analysis on the effect of short-chain branches on the structure and dynamics of interfacial chains in comparison with the corresponding linear polymer, two different monodisperse PE melts were employed in this study[34]: $C_{128}H_{258}$ linear PE and $C_{178}H_{358}$ SCB PE systems, where each SCB molecule contains 128 carbon atoms in the backbone (the same as the linear polymer) and 10 short branches (uniformly distributed along the backbone) with each containing 5 carbon atoms. Canonical NEMD simulations were carried out at constant temperature T = 450 K with density ρ = 0.7684 g/cm^3 for the linear, and ρ = 0.7745 g/cm^3 for the SCB systems (corresponding to the pressure P = 1atm for both systems), by using the p-SLLOD algorithm[6,7] implemented by a Nosé-Hoover thermostat[8,9] and the standard Lees-Edwards sliding-brick boundary conditions[13] in wide range of flow strengths, corresponding to Weissenberg numbers Wi: $1.76 \le Wi \equiv \tau\dot{\gamma} \le 4410$ with τ = 20.7 ± 4.5 ns for the linear PE and $6.04 \le Wi \equiv \tau\dot{\gamma} \le 7550$ with τ = 35.5 ± 7.2 ns for the SCB PE melts. The set of evolution equations was numerically integrated via the r-RESPA[10] with two different MD time steps: 0.48 fs for the three bonded (bond-stretching, bond-bending, and bond-torsional) interactions and 2.39 fs for the nonbonded inter- and intramolecular LJ interactions, using the well-known TraPPE[12] united atom model. The surface energy of the walls for all the PE systems was set as the LJ energy parameter ε_w/k_B = 939K,[35] which is comparable to that of a mica surface (~200-400mJ/m^2).

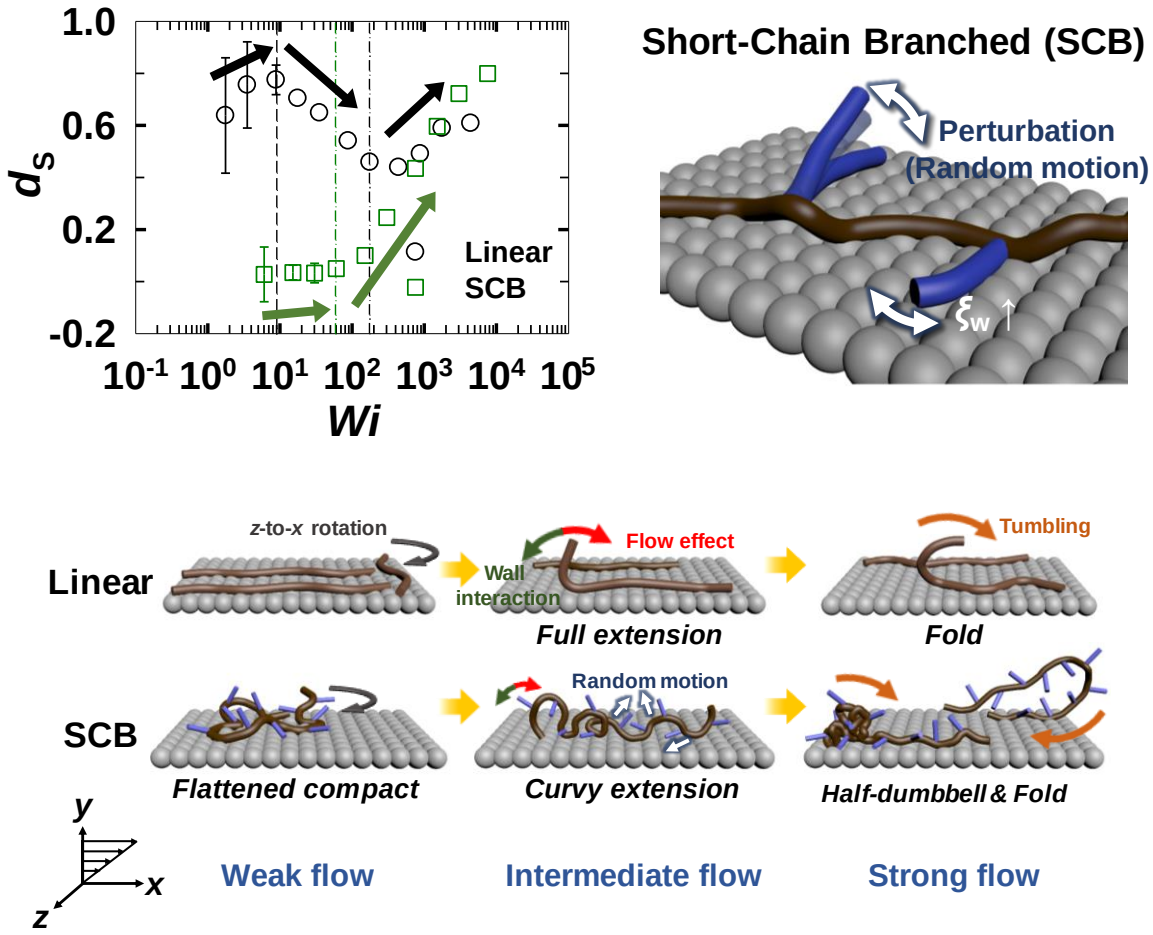

Figure 4.1.3. (Top) Variation in the degree of slip (d_s) as a function of *Wi* for the simulated linear and SCB polyethylene melts. The vertical lines separate the respective characteristic flow regimes with respect to d_s for each system. The error bars are smaller than the size of the symbols unless otherwise specified. Right panel represents sketch of the representative orientations of short-chain branches near the solid surface. ξ_w denotes the (average) friction coefficient of polymer segments exerted by the wall. (Bottom) Schematic description of the characteristic molecular structure and dynamic mechanisms of interfacial chains for the linear and SCB polymers in each flow regime.

First, the degree of slip (d_s) with applied flow strength is plotted in right top panel in Fig. 4.1.3. In contrast to the three distinctive characteristic regimes in the degree of slip observed by the linear polymer [increasing, decreasing, and increasing tendencies in the weak, intermediate, and strong flow regimes, respectively (see Fig. 4.1.2)], the SCB polymer exhibits an almost constant value of d_s in the weak-to-intermediate flow regimes, then rapid increasing behavior of d_s with *Wi*. As mentioned, the increasing tendency of d_s in the weak flow regime for the linear polymer is ascribed to the *z*-to-*x* in-plane chain rotation, enhancing the slip via reduction of the interfacial friction against the wall in the flow direction. Such a characteristic is, however, not distinct in the case of the SCB polymer. This seemingly is related with the fact that the overall dynamic friction of interfacial SCB polymer is dominated by the attached short branches, as well as the chain backbone. The short branches tend, on average, to be oriented more perpendicular to than parallel to the backbone, referred to right top panel in Fig. 4.1.3. Therefore, via the *z*-to-*x* rotational mechanism, whereas the polymer-wall friction contributed by the chain backbone is reduced, that contributed by the short branches is increased; these two contrasting factors effectively cancel each other out to result in almost constant d_s in the weak flow regime for the SCB polymer. This is clearly identified in Fig. 4.1.4, where it shows the *xx*-component of the gyration tensor $\mathbf{G}^{\mathbf{inf}}$ for the interfacial chains as a function of *Wi* number. The linear polymer exhibits a gradual increase in $G_{xx}^{\inf}$ with shear rate in the weak flow regime via the *z*-to-*x* rotational mechanism, whereas the SCB polymer displays continuously increasing $G_{xx}^{\inf}$ throughout the weak-to-intermediate flow regimes. This can be understood by considering that interfacial SCB chains become oriented in the *x*-direction but with a rather compact (less deformed) with increasing flow strength in the weak-to-intermediate flow regimes, thus leading to a slower increase in d_s in the weak-to-intermediate flow regime.

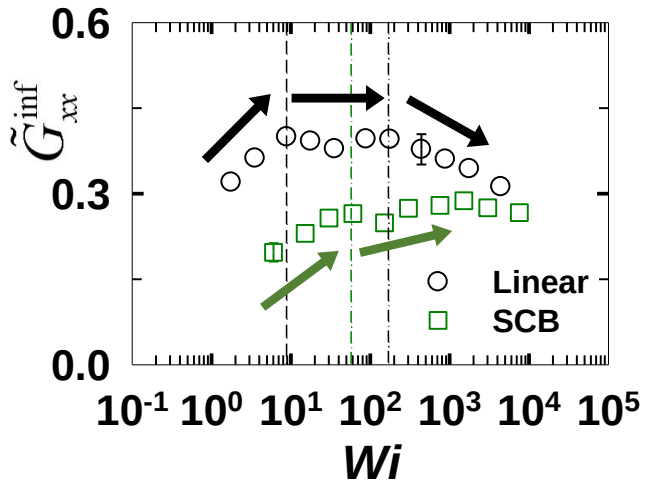

Figure 4.1.4. Plots of the *xx*-component of the gyration tensor $\mathbf{G}^{inf}$ (normalized by the fully-stretched backbone length) for the interfacial chains only (chains whose center-of-mass is located within 2.5 σ from the wall surface) for the simulated linear and SCB PE melts. The vertical lines separate the respective characteristic flow regimes with respect to d_s for each system. The error bars are smaller than the size of the symbols unless otherwise specified.

Dynamics of the highly mobile short branches are considered to be essentially unaffected by the flow field, as their characteristic time scale is generally much shorter than that of the practically applied flow field. For instance, based on the Rouse theory for unentangled polymer melts, the characteristic relaxation time τ of the melt system consisting of C_5H_{12} (~5 CH_2 units) short branches whose one chain end is fixed (i.e., each branch is tethered on a relatively long backbone in this study) can be approximately equal to that of the $C_{10}H_{22}$ (~10 CH_2 units) PE melt at the corresponding state point. Thus τ for the short branch is very small compared to the longest relaxation time for the SCB PE melts and the applied flow time scales. The random movements of the short branches constantly disturb the stable chain conformation, causing the overall chain structure to be more compact at equilibrium and less vulnerable to deformation (i.e., less oriented and stretched) in response to the imposed flow. This gives rise to an overall lesser degree of intermolecular entanglement between chains at equilibrium and a less variation in the degree of entanglement with flow strength. Thus, in the intermediate flow regime the SCB polymer, compared to the linear polymer, exhibits relatively weaker (smaller magnitude of wagging motion) out-of-plane wagging interfacial chain dynamics, in conjunction with a less deformed structure against the flow field (Fig. 4.1.4). Diminished out-of-plane wagging motion for the SCB polymer can be identified in Fig. 4.1.5, where These structural and dynamical features of the SCB polymer underlie a very small variation of d_s even in the intermediate flow regime (see middle picture of bottom panel in Fig. 4.1.3). Consequently, the dual effects of short branches lead to the apparent constant behavior of d_s throughout the weak-to-intermediate flow regimes.

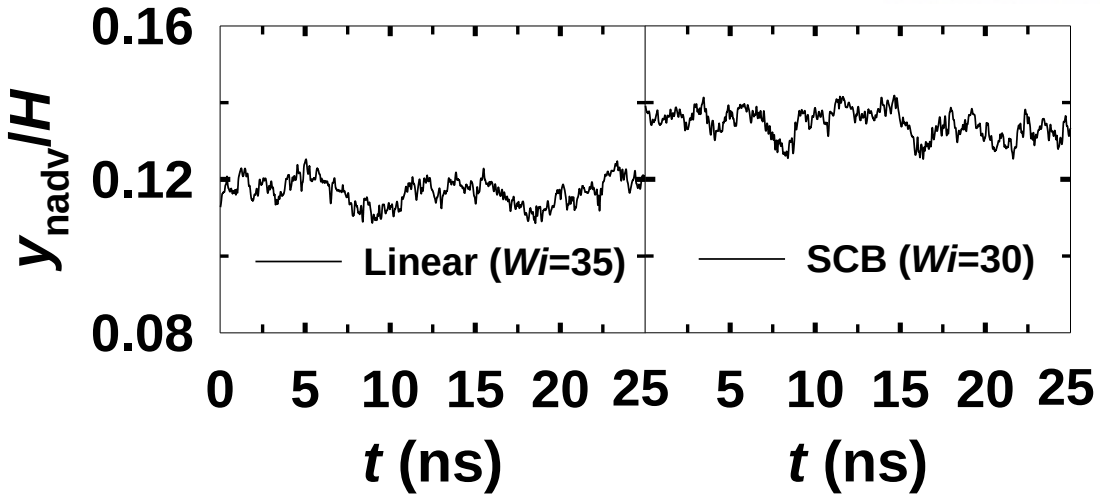

Figure 4.1.5. Average *y*-position (divided by the channel height *H*) for the center-of-mass of the non-adsorbed parts (y_{nadv}) of the interfacial chains as a function of time for the linear and SCB PE melts at an intermediate flow strength.

With a further increase of flow strength (strong flow regime), both the linear and SCB polymers exhibit a significant increase in d_s with increasing shear rate. This behavior is associated with irregular chain rotation and tumbling dynamics[33] via intensive dynamical collisions of interfacial chains against the wall. However, in comparison to the linear polymer, the SCB polymer exhibits a steeper increase in d_s. This is attributed to an enhancement effect on the chain detachment from the wall via the highly mobile random motions of short branches along the backbone. Most importantly, we have identified a very distinctive molecular dynamic mechanism exposed by the SCB polymers in the strong flow regime. Figure 4.1.6 presents the characteristic molecular mechanism of interfacial chains for the linear and SCB polymers at high flow strengths in conjunction with the mesoscopic structural analysis via the Brightness method,[36,37] which categorizes the mesoscale chain structures into several representative configuration classes (i.e., Coil, Fold, Kink, Dumbbell, Half-dumbbells, and Stretched) based on the monomer distribution along the chain, focusing on the overall chain configuration or shape without regard to the actual chain size. The linear polymer exhibits well-defined hairpin-like tumbling behavior (respecting the geometrical constraint imposed by the wall) featured by the conformational transition of Stretched→Fold→Stretched. In sharp contrast, the SCB polymer exhibits not only the hairpin-like tumbling behavior, but also two distinct rolling dynamics beginning with either a compact head or tail part (i.e., head-roll and tail-roll tumbling mechanisms). Both of these are featured by the major conformational transition of Stretched→Half-dumbbell→Coil→Half-dumbbell→Stretched during a tumbling cycle (instantaneous snapshots representing the distinct tumbling mechanisms of the linear and SCB polymers are presented in bottom panel in Fig. 4.1.6). The frequent occurrence of the Half-dumbbell conformation in the SCB polymer is ascribed to the random motions of the short branches in addition to the free motions of the chain ends. The SCB polymer with the Half-dumbbell conformation tends to roll up along its backbone on the wall and then attains a coiled structure during tumbling.

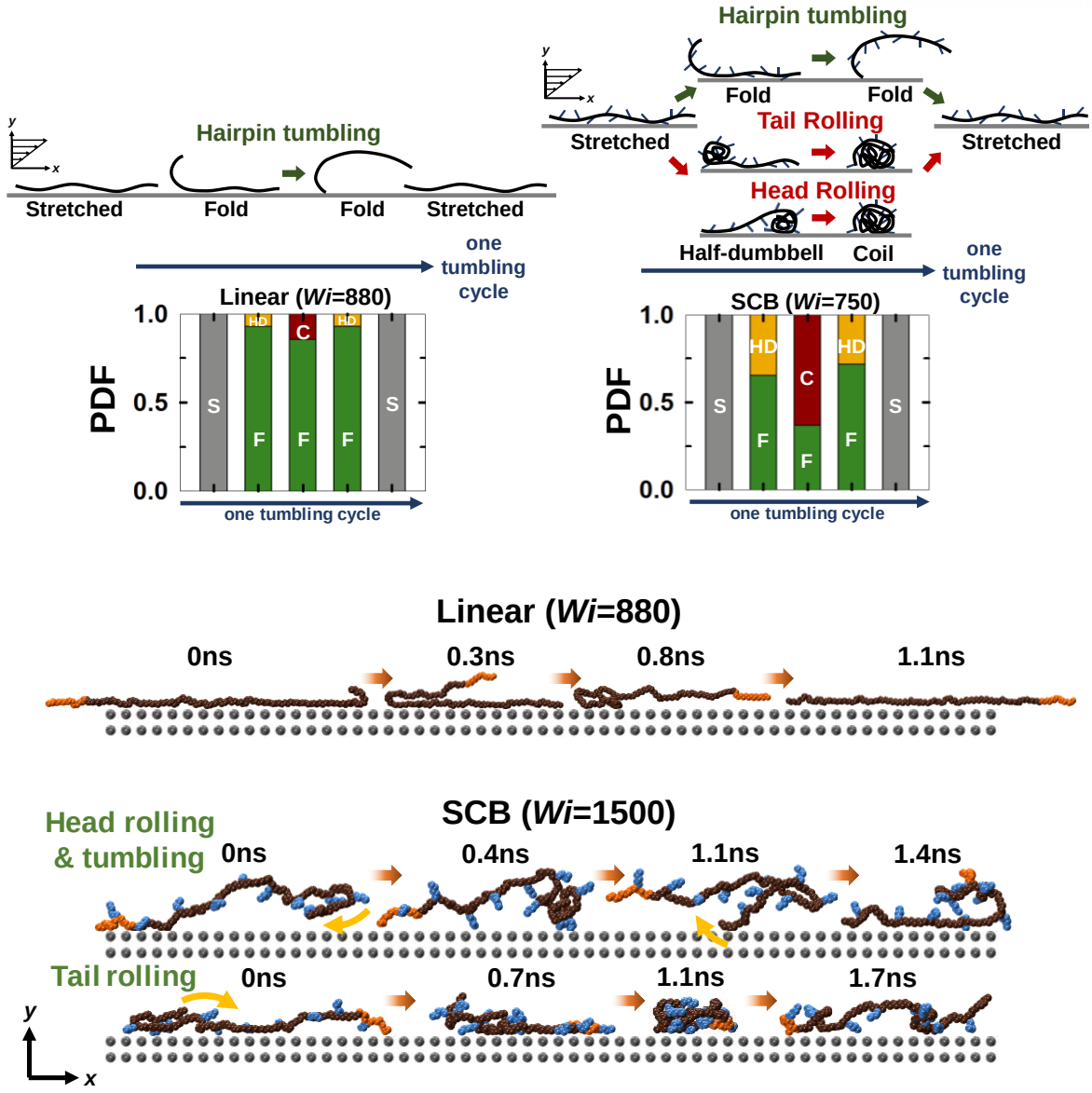

Figure 4.1.6. (Top) Schematic illustration of the characteristic molecular mechanism of the interfacial chains at high flow fields and the probability distribution function (PDF) of the representative mesoscopic chain conformations [Stretched (S), Fold (F), Half-dumbbell (HD), Coil (C)] obtained by the Brightness analysis during a tumbling cycle for the linear and SCB PE systems. (Bottom) Snapshots of a selected interfacial chain, describing the representative tumbling mechanisms for the linear and the SCB polymers under strong flow.

4.1.4 Ring (cyclic) polymer melts

Ring polymer, characterized as a linear polymer albeit with an internally closed-loop molecular geometry (obviating the chain ends), has attracted special attention in the field of polymer rheology.[1,38-47] The intrinsic geometrical constraint of ring topology induces various distinctive structural and rheological features for ring systems, compared with the linear analogues.[38-46] Based on these intriguing physical aspects of ring polymers, a detailed NEMD study of the interfacial structural and rheological properties of confined ring melts under shear has conducted. Particular focus was placed on the analysis of the fundamental molecular characteristics underlying the distinctive structural and dynamical behaviors of ring polymer melts in response to the applied flow strength.

Two sets of PE melts, C_{128} and C_{400} monodispersed (unconcatenated and unknotted) ring and linear PE melts, were employed.[48] The atomistic Canonical NEMD simulations were carried out at a constant temperature T = 450 K for all the systems with densities ρ = 0.7684 g/cm^3 and 0.7294 g/cm^3 for the $C_{128}H_{258}$ and $C_{400}H_{802}$ linear PE systems, respectively, and ρ = 0.7700 g/cm^3 and 0.7390 g/cm^3 for the $C_{128}H_{256}$ and $C_{400}H_{800}$ ring PE systems, respectively (corresponding to the pressure P = 1 atm for each system). The well-known TraPPE[12] and SKS united atom model[11] were adopted in the simulations. The lattice parameter of the simple cubic wall was set equal to 5.227Å, corresponding to the Lennard–Jones (LJ) size parameter $\sigma_w = 1.33\ \sigma_f$ ($\sigma_f = \sigma_{CH2}$). The surface energy of the walls for all the PE systems was set as the LJ energy parameter ε_w/k_B = 939K,[34] which is comparable to that of a mica surface (~200–400mJ/m^2). The interfacial chains for each confined system in this study are defined as the chains whose center-of-mass is located within 2.5 σ from the wall surface. The NEMD simulations for shear flow were executed with the p-SLLOD algorithm[6,7] implemented by a Nosé–Hoover thermostat[8,9] and the standard Lees–Edwards sliding-brick boundary conditions.[13] The set of evolution equations was numerically integrated using an efficient r-RESPA[10] with two different MD time steps: 0.48 fs for the three bonded (bond-stretching, bond-bending, and bond-torsional) interactions and 2.39 fs for the nonbonded inter- and intramolecular LJ interactions, the thermostat, and the flow field. A wide range of flow strengths spanning from linear to highly nonlinear viscoelastic regimes was applied in each system, corresponding to Wi such that $1.76 \le Wi \le 4410$ with τ = 20.7 ± 4.5 ns for the C_{128} linear, $45 \le Wi \le 117800$ with τ = 525 ± 12 ns for the C_{400} linear, $1.09 \le Wi \equiv \tau\dot{\gamma} \le 544$ with τ = 2.55 ± 0.4 ns for the C_{128} ring, and $0.91 \le Wi \equiv \tau\dot{\gamma} \le 2282$ with τ = 10.9 ± 1.1 ns for the C_{400} ring PE melts.

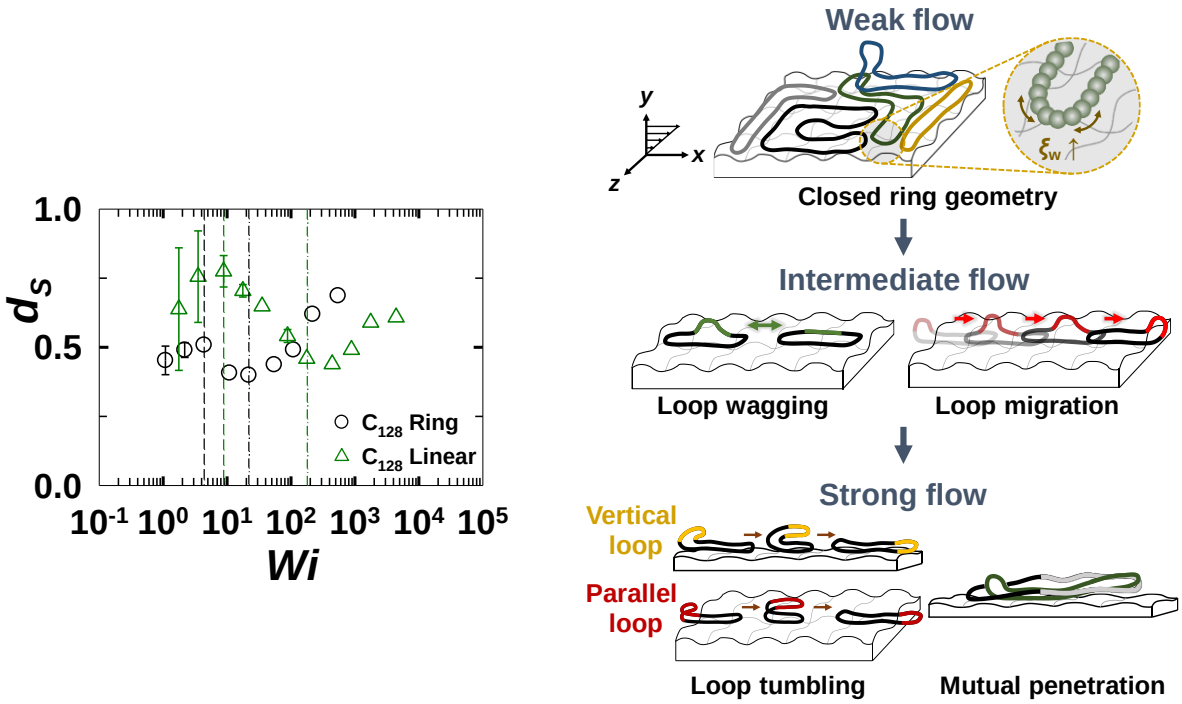

Figure 4.1.7. Degree of slip and the associated characteristic molecular mechanisms. (Left) Variation of degree of slip (d_s) as a function of *Wi* number for the simulated C_{128} ring and linear polyethylene (PE) melts. The vertical lines separate the three (weak, intermediate, and strong) representative flow regimes with respect to d_s for each system. The error bars are smaller than the size of the symbols unless otherwise specified. (Right) Schematic description of the characteristic molecular mechanism(s) of interfacial ring chains for each flow regime. Here the loop is a chain section comprised of the atoms located over one atomic layer from the wall surface.

Left panel in Fig. 4.1.7 shows the variation of the degree of slip (d_s) for the $C_{128}H_{256}$ linear and ring polyethylene melts as a function of *Wi*. Both systems exhibit three distinctive characteristic regimes (increasing, decreasing, and increasing behaviors in the low, intermediate, and high flow regimes, respectively) with respect to the degree of slip. In the weak flow regime, d_s increases for both systems with increasing *Wi* number. This behavior is directly associated with the (in-plane) *z*-to-*x* chain rotation from the neutral (*z*-)direction to the flow (*x*-)direction with increasing flow strength, which effectively decreases the dynamic friction of polymer chains against the wall in the flow direction and thus enhances the interfacial slip (also found in previous studies[33,34]). However, not only the magnitude of d_s but also its increasing tendency appears to be smaller for the ring polymer compared to the linear analogue, indicating a larger polymer-wall friction and a smaller degree of frictional reduction via the *z*-to-*x* rotation mechanism for the ring system than for the linear system. This phenomenon can be elucidated that the ring polymer, due to its intrinsic closed-loop topology, has a smaller chain extension in the flow (*x*-)direction under shear in comparison with the corresponding linear polymer (right panel in Figure 4.1.7; see also Figure 4.1.8 below). Accordingly, the relatively larger chain dimension in the neutral (*z*-)direction at the interface gives rise to a larger wall friction. Furthermore, the structural compactness (in association with the built-in ring topology) against the applied flow would result in a lesser degree of chain stretch and alignment to the flow direction and thus a smaller frictional reduction for the ring system via the *z*-to-*x* rotation in the weak flow regime as compared to the linear polymer.

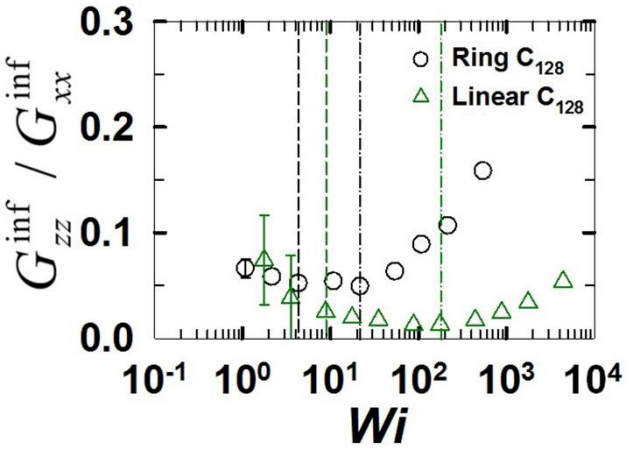

Figure 4.1.8. Plots of the ratio between the *xx* and *zz* components of interfacial gyration tensor $\mathbf{G}^{inf}$ (whose calculation involves only the chains that have their center-of-mass below 2.5 σ from the wall) for the simulated C_{128} ring and linear polyethylene (PE) melts. The superscript 'inf' in $\mathbf{G}^{inf}$ indicates 'interfacial'. The vertical lines separate the three characteristic flow regimes. The error bars are smaller than the size of the symbols unless otherwise specified.

In the intermediate flow regime, the degree of slip is seen to decrease with increasing flow field for both ring and linear PE melts; however, d_s still appears smaller for the ring than the linear system. As found in previous works,[33,34] the behavior of d_s for the linear polymer in this regime is associated with two fundamental molecular mechanisms: (i) the out-of-plane chain wagging dynamics, and (ii) the disentanglement mechanism between the interfacial chains and nearby surrounding bulk chains. Although such wagging dynamics is also observed for the ring polymer, it occurs at any places within a loop (i.e., a chain section consisting of the atoms located over one atomic layer from the wall surface) along the ring chain (middle picture of right panel in Figure 4.1.7) in contrast to the linear polymer where the wagging occurs predominantly at the outer chain sections near the chain ends; it is thus called the loop wagging mechanism for ring polymer. More interestingly, the ring systems exhibit an additional dynamical mechanism (called the loop migration) where the loop(s) can propagate along the chain (middle picture of right panel in Figure 4.1.7; see also Figure 4.1.9). This mechanism results in a movement of the chain center-of-mass in the flow direction, thus making a contribution to the polymer slip at the wall. It can be seen that the loops exhibit a repetitive motion between detachment from the wall and attachment to the wall as a result of combined effects of the external flow field (inducing loop detachment) and the favorable (attractive) polymer-wall interaction (inducing loop attachment) in the course of loop wagging as depicted in Fig. 4.1.9. By contrast, in the case of the loop migration mechanism (right panel in Fig. 4.1.9), the loops move (i.e., the perturbed parts propagate) along the chain toward the flow direction. It can be expected that as the external flow field promotes the loop propagation (as well as the loop creation) by overcoming the attractive polymer−wall interaction, the loop migration dynamics would become more dominant over the loop wagging dynamics with increasing flow strength. Result of the probability distribution function (PDF) for these two loop mechanisms (directly calculated by tracking down the individual loop motion) confirms this behavior (top panel in Figure 4.1.10). It is evident that as the shear rate increases in the intermediate flow regime, the PDF of loop migration gradually increases whereas that of loop wagging decreases significantly. It is further seen that the loop migration velocity along the chain is approximately proportional to the applied flow strength in this regime (bottom panel in Figure 4.1.10). Although it seems to be naively expected, the linear proportionality between the loop migration velocity and the applied flow indicates that the structural and dynamical characteristics of loops do not vary much with the flow strength in the intermediate flow regime, beyond which under strong flow fields, however, the loop structure and dynamics significantly change and fluctuate irregularly with time, depending on the flow strength. Therefore, this phenomenon, together with relatively less topological (entanglement) interactions between ring chains than linear chains, consequently leads to a lesser degree of the decreasing tendency of slip for the ring polymer in comparison with the linear polymer in the intermediate flow regime, as shown in Figure 4.1.7.

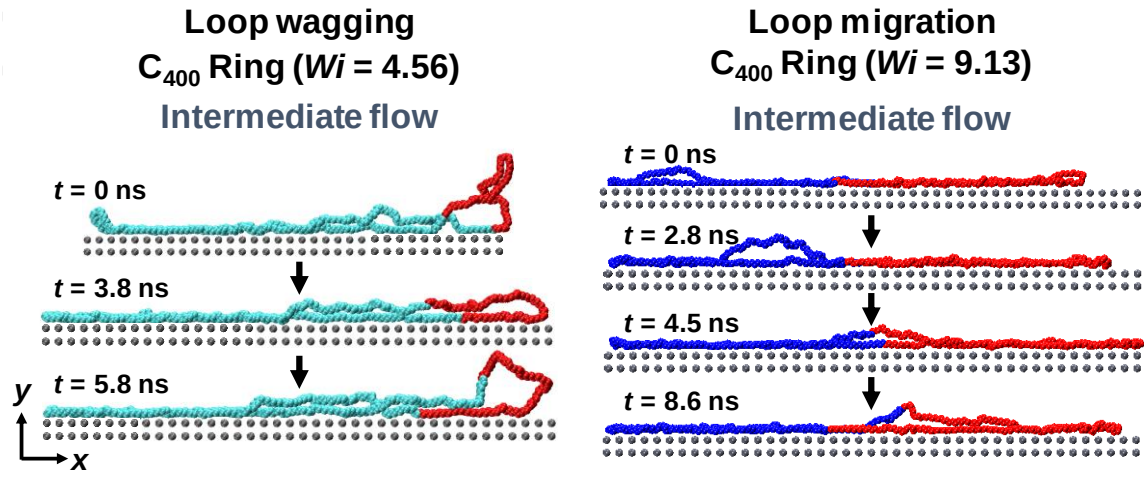

Figure 4.1.9. Snapshots of a selected interfacial chain for describing the characteristic molecular mechanisms (loop wagging and loop migration) for the C_{400} ring system in the intermediate flow regime.

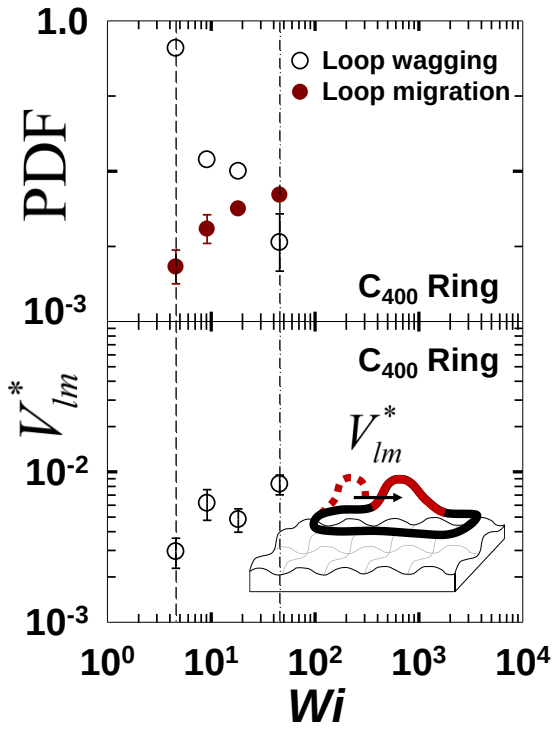

Figure 4.1.10. Probability distribution function (PDF) of the loop wagging and loop migration mechanisms exhibited by the interfacial chains (top panel) and the (reduced) loop migration velocity $V_{\mathrm{lm}}^{*}\left(=V_{\mathrm{lm}}\Big/\sqrt{\varepsilon_{\mathrm{CH_2}}/m_{\mathrm{CH_2}}}\right)$ along the chain (bottom panel) for the C_{400} ring PE melt in the intermediate flow regime. Here the PDF represents the number of interfacial chains exhibiting either the loop wagging or migration dynamics as normalized by the total number of interfacial chains. We also note that some interfacial chains do not reveal any of such loop dynamics and others show both loop wagging and migration dynamics.

In the strong flow regime, d_s exhibits a rapid increase with increasing flow strength for both ring and linear systems. The characteristic molecular mechanism behind this phenomenon is the highly nonlinear, irregular (chaotic) chain rotation and tumbling dynamics via strong dynamical collisions of interfacial chains with the wall.[30,31] Once the outer part is sufficiently perturbed and detached from the wall, the flow strongly promotes further detachment of the part from the wall and its movement in the flow direction simultaneously with dragging the remaining parts of chain, leading to a typical hairpin-like chain tumbling behavior.[44] While such mechanism appears in both systems, the ring polymer exhibits distinctive molecular characteristics compared to those of the linear polymer. First, ring polymer exhibits a loop-induced tumbling dynamics along the chain, whereas tumbling occurs exclusively with chain ends for linear polymer. Secondly, two different types of loop tumbling (parallel and vertical; see Figure 4.1.11) appear for the ring polymer, depending on the orientation of the loop-section plane with respect to the *z*-*x* interfacial (or vorticity) plane. Whereas the loop plane aligns in parallel to the *x*-*z* (vorticity) plane in the case of parallel loop tumbling, it aligns in parallel to the *x*-*y* (shear) plane for the vertical loop tumbling. Therefore, the parallel loop-tumbling would generally experience a structurally higher polymer-wall interaction (and the concomitant dynamic friction) in comparison with the vertical one. As such, their relative probability is supposed to be dependent on the applied flow strength. Figure 4.1.12 presents the probability distribution with respect to the angle (θ_{loop}) of the loop-section plane with respect to the *x*-*z* plane (i.e., θ_{loop} is equal to 0° for the perfectly parallel loop and 90° for the perfectly vertical loop). It is seen that the parallel loop tumbling becomes increasingly favorable over the vertical one as the flow strength increases (Figure 4.1.12). This is because under strong flow fields even the short local chain sections tend to be more aligned in the flow direction with increasing shear rate. We mention in the passing that complex tumbling behaviors can be observed with frequent θ_{loop} changes even during one tumbling cycle, e.g., as a sequential transition between the parallel and vertical loops).

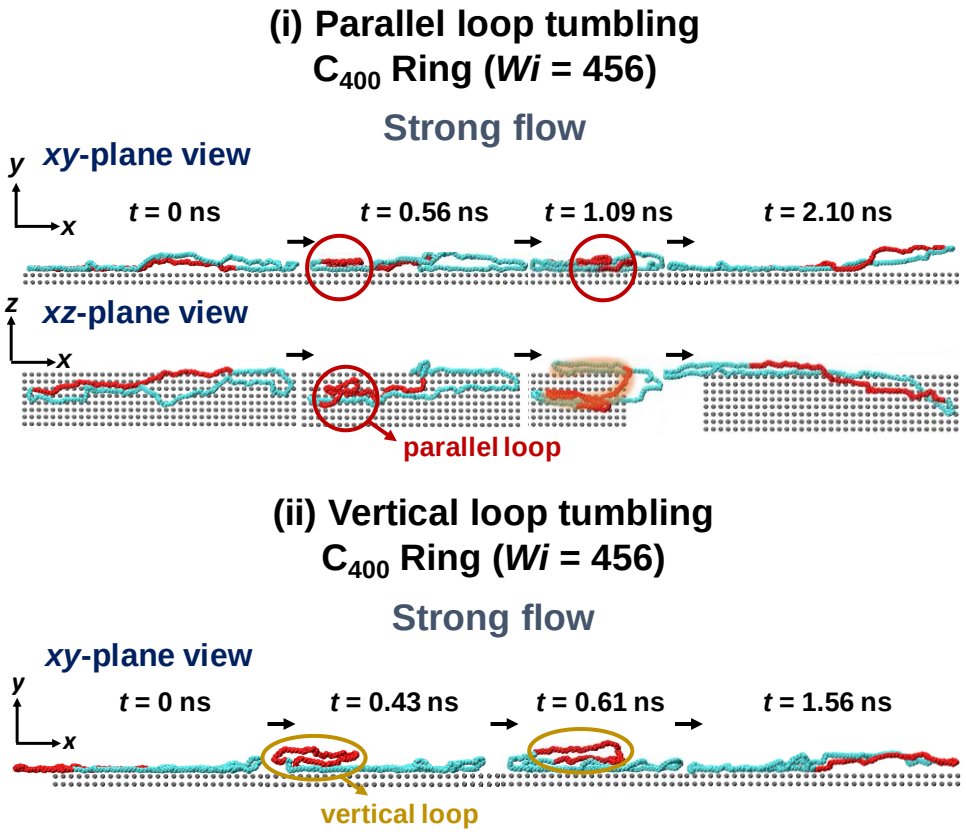

Figure 4.1.11. Snapshots of a selected interfacial chain for describing the representative molecular mechanisms (parallel and vertical loop tumbling) exhibited by interfacial chains for the C_{400} ring system under strong flow fields, depending on the angle of the loop-section plane relative to the *x*-*z* interfacial plane (i.e., the loop plane aligns in parallel to the *x*-*z* (vorticity) and the *x*-*y* (shear) planes for the parallel and vertical loop tumbling, respectively). The red circles indicate the loop sections involved in tumbling dynamics.

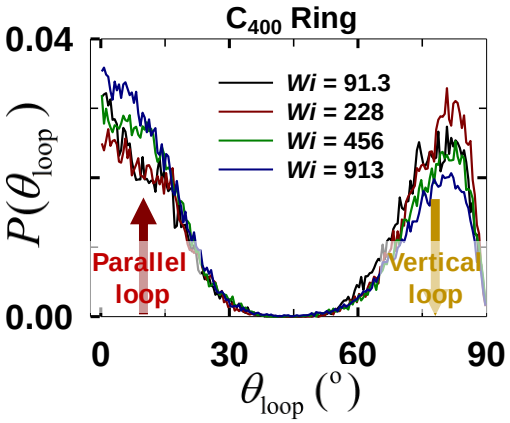

Figure 4.1.12. Probability distribution of the angle (θ_{loop}) of the loop-section plane with respect to the *x*-*z* plane.

Additional distinctive molecular feature, which is the mutual penetrations between interfacial chains, has been further identified for ring melts under high flow fields. Since the mutual threading or entanglement between chains is likely to change the effective molecular weight of the moving chain, the interfacial chain dynamics and slip behaviors can be significantly affected by this phenomenon. Figure 4.1.13 (top panel) presents the average number N_{penet} of the penetrating interfacial chains per interfacial chain as a function of flow strength. Interestingly, N_{penet} of interfacial chains gradually decreases with increasing *Wi* in the intermediate regime, but exhibits a rather steep increase for further increasing *Wi* in the strong flow regime. Therefore, an interfacial chain is likely to frequently move together with other nearby interfacial chains especially in the strong flow regime, implicating that the effective molecular weight of interfacial chain is increased and becomes larger at higher flow strengths. This dynamical feature appears to become more significant as the chain length increases, because the effective surface area available for penetration by other chains increases for a longer interfacial ring chain. We also measured how long, on average, such mutual penetration remains (t_{penet}). As shown in Figure 4.1.13 (top panel), t_{penet} as well as N_{penet} increases significantly with increasing flow strength in the strong flow regime (i.e., amounting to ~10–20% of the total interfacial residence time). In conclusion, since the mutual coupling between interfacial chains may alter the effective molecular weight of a moving interfacial chain thereby affecting various interfacial properties such as slip, in-plane and out-of-plane diffusion of interfacial chains, and heat dissipation at the interface, we propose that the dynamical coupling between interfacial chains at high flow fields should be considered an important rheological characteristic in analyzing confined ring polymer systems. Figure 4.1.13 (bottom panel) presents representative atomistic snapshots that illustrate such mutual coupling behaviors between interfacial chains occurring in tumbling dynamics at high flow strength (i.e., *Wi*=456). In this example, while a ring molecule executes a typical rotational motion at the interface, the chain tumbling is considered to be less efficient as the chain is physically coupled with another nearby interfacial chain.

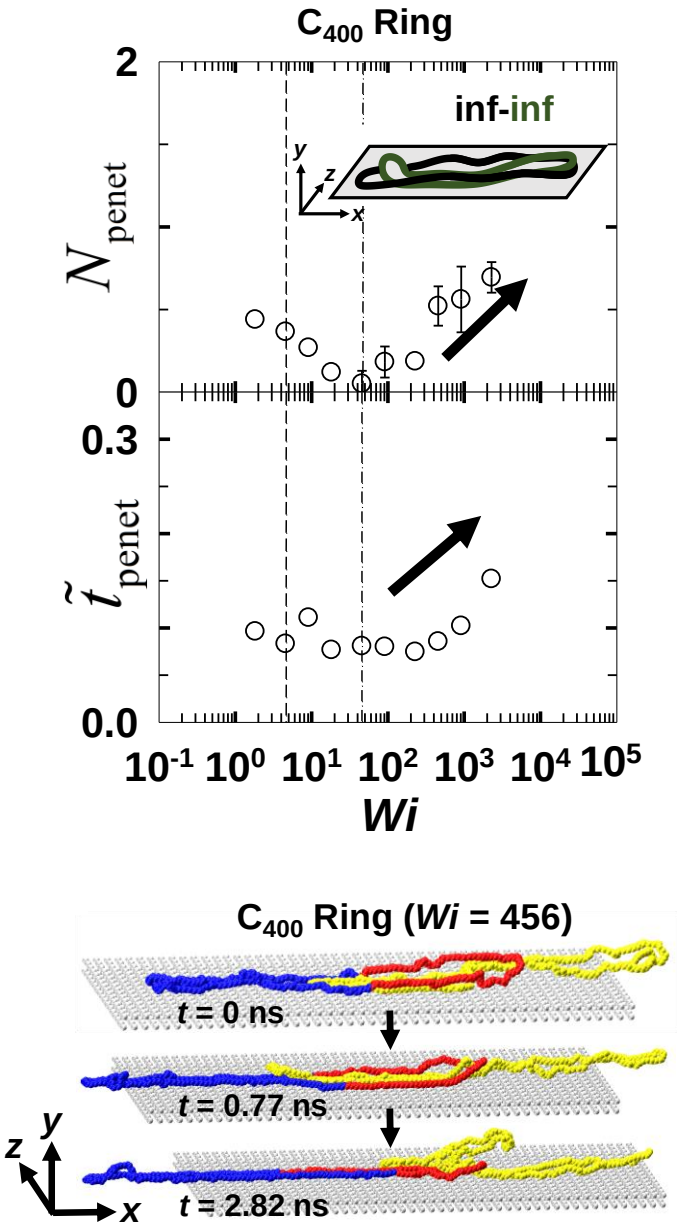

Figure 4.1.13. Mutual penetration behaviors between interfacial ring chains under strong flow fields. (Top) Average number N_{penet} of penetrating interfacial chains per interfacial chain (top panel) and penetration time t_{penet} (bottom panel), as a function of shear rate for the C_{400} ring melt. Here t_{penet} (the average time-length for which the mutual penetration remains) was normalized by the total interfacial residence time [the average time-length for which an interfacial chain resides inside the interfacial region (within 2.5 σ from the wall surface)]. To compute N_{penet} and t_{penet}, we first analyzed the adsorbed area of individual interfacial chains on the wall. We then directly measured how many other interfacial chains are penetrated within the area. Since the mutual penetration between interfacial chains requires a closed space for a reference chain to trap other chains, it is a unique phenomenon for ring polymers bearing the intrinsic characteristic of a closed-loop conformation. Furthermore, this feature become larger with increasing chain length, because the closed surface area increases for longer ring chains; e.g., N_{penet} and t_{penet} for the C_{128} ring PE melt (not shown here) are found to be much smaller than those for the C_{400} ring PE melt. (Bottom) Snapshots of two selected interfacial chains for describing how the mutual penetration behavior occurs and evolves with time for the C_{400} ring melt under strong flow.

4.2 Polymer melts undergoing start-up shear flow

Stress overshoot, exhibited by polymeric liquids undergoing start-up shear above a certain critical flow strength, is a phenomenon that the shear stress (or viscosity η) of the system initially increases with time, then reaches a maximum value accompanied by a decrease, and eventually attains a steady-state value. This overshoot peak is generally observed at strain values $\gamma_{\eta}^{\max} \approx 2-3$, regardless of the polymer type and the applied shear rate (a similar behavior has been also found in the first normal stress coefficient Ψ_1, but for a higher value of peak strain, $\gamma_{\Psi_1}^{\max} \approx 2\gamma_{\eta}^{\max}$).[14-16] Flow birefringence has been widely well-known in the field of polymer rheology for properly describing stress behaviors for sheared polymeric liquid (known as stress-optical rule, SOR). According to the tube theory[1,17-19] for entangled polymeric materials, the SOR is valid in the range of strain rates $\tau_d^{-1} < \dot{\gamma} < \tau_R^{-1}$, where τ_d and τ_R are the terminal relaxation time and the Rouse time, respectively. This implies that, in such flow range, the stress overshoot would be effectively related to segmental orientation of entangled polymers, as also identified by experimental studies.[18,20] In this study,[21,22] we conducted direct NEMD simulations of an entangled polymer melt ($C_{400}H_{802}$ linear PE) under simple shear flow. Canonical NEMD simulations were carried out at constant temperature T = 450 K and density ρ = 0.7640 g/cm^3, using the well-known *p*-SLLOD algorithm[6,7] implemented by a Nosé-Hoover thermostat[8,9] and the standard Lees-Edwards sliding-brick boundary conditions.[13] The set of evolution equations was numerically integrated using *r*-RESPA.[10] The well-known SKS[11] united-atom potential model was utilized in the simulations, with the exception that the rigid bond adopted in the original model was replaced by a flexible one described through a harmonic potential. For a thorough exploration of the structural and dynamical characteristics of stress overshoot, we applied a wide range of flow strengths, corresponding to Weissenberg numbers Wi_d and Wi_R (defined as the product of the characteristic relaxation time τ of the system and the imposed strain rate) satisfying $3.71 \le Wi_d \equiv \tau_d\dot{\gamma} \le 928$ or $0.91 \le Wi_R \equiv \tau_R\dot{\gamma} \le 229$, with τ_d = 218 ± 10 ns[23] and τ_R = 53.7 ± 10 ns[21] for the $C_{400}H_{802}$ PE melt system.

4.2.1 Transient behaviors of properties

Figure 4.2.1 shows the transient behaviors of stresses, birefringence and entanglement orientation tensors of entangled polymer melts undergoing start-up shear at sufficiently high flow field. Consistently with previous studies,[24-26] it is observed that the overshoot occurs at strain values around 2-3, with tendency of increasing the peak strain value and magnitude of the peak with increasing strain rate. Importantly, it also reveals the well-known stress-optical relationship between the shear stress and the corresponding birefringence. In addition to the birefringence, we analyzed the transient behavior of the order (or orientation) tensor $\mathbf{S}$ of entanglement strands along the chains in association with the tube theory for entangled polymers, defined as:

$$S_{\alpha\beta} = \frac{1}{N_{seg}} \sum_{i=1}^{N_{seg}} \left\langle \frac{(r_{i+1} - r_i)_\alpha (r_{i+1} - r_i)_\beta}{(\mathbf{r}_{i+1} - \mathbf{r}_i)^2} \right\rangle \tag{4.2.1}$$

where $\mathbf{r}_i$ denotes the end-to-end vector of the i^{th} entanglement strand and N_{seg} the total number of entanglement strands. For this purpose, we generated the entanglement network corresponding to the modeled system via the well-known Z1-code.[27,28] In addition, we also calculated the order tensor based on the entanglement strands connecting the two centers of mass of neighboring subchains, formed by dividing a chain into six subchains based on the known experimental value for the number N_e of carbon atoms per entanglement strand (N_e = 68 for polyethylene[29]). Note that the transient behavior of the orientation tensor of entanglement strands appears very similar to that of the stress and the birefringence tensor. Thus the present results show the chain orientation, rather than the overall chain stretching, is the dominant molecular mechanism behind the macroscopic stress overshoot. We also notice that the overshoot peak is almost completely absent in the $S_{xx} - S_{yy}$ plot: this is mainly ascribed to the definition of the orientation tensor (eq. 4.2.1), based on the unit end-to-end vector of an entanglement strand, as the magnitude of $S_{xx} - S_{yy}$ is considerably affected by the segment stretch.

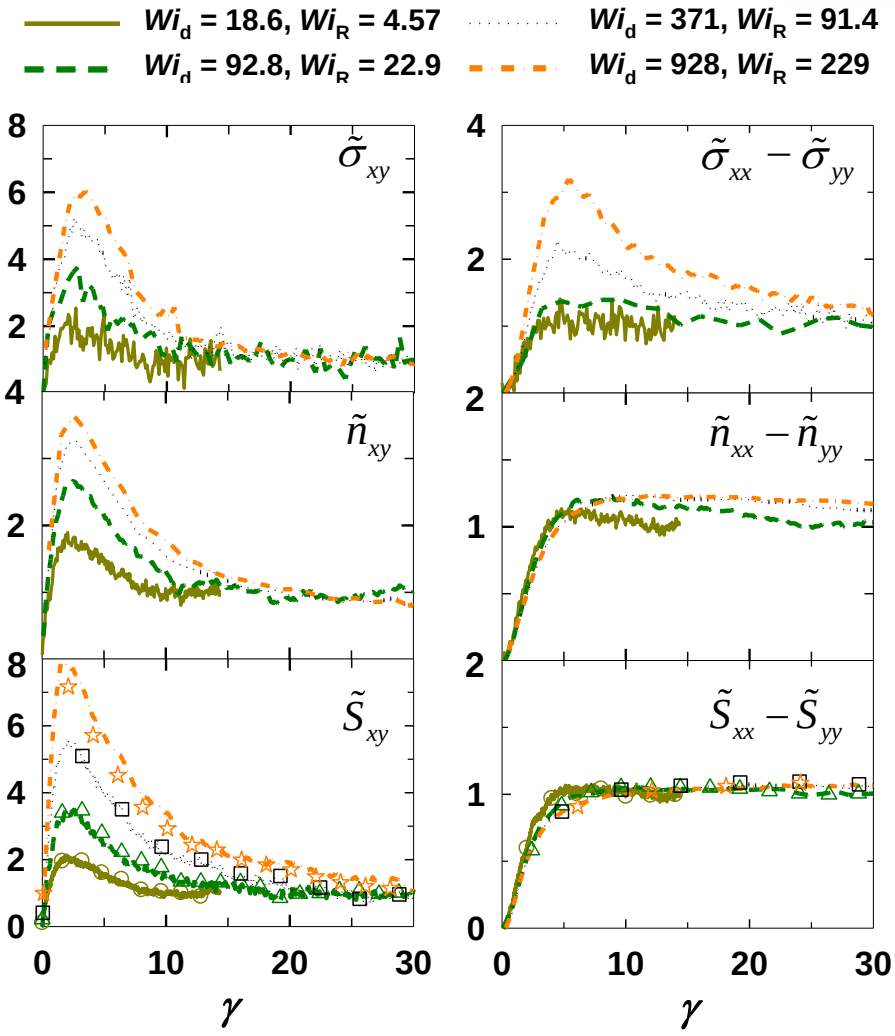

Figure 4.2.1. Transient behavior of stress **σ**, birefringence **n**, and entanglement segment orientation **S** (eq. 4.1.1), as a function of strain for the simulated $C_{400}H_{802}$ polyethylene melt under start-up shear at four different flow strengths: $Wi_d = 18.6$ and $Wi_R = 4.57$ (dark yellow solid lines), $Wi_d = 92.8$ and $Wi_R = 22.9$ (dark green dashed lines), $Wi_d = 371$ and $Wi_R = 91.4$ (black dotted lines), and $Wi_d = 928$ and $Wi_R = 229$ (orange dashed-dotted lines). The lines and symbols in bottom panel represent the orientation tensor results calculated from the entanglement network obtained with the Z1-code[27,28] and with the number of carbon atoms per entanglement strand (N_e) set to 68, respectively (see the text for details). All properties are normalized (as indicated by the tilde symbol) by their steady-state value.

We now directly compare the birefringence and the shear stress under start-up shear flow at four different shear rates, as shown in Figure 4.2.2. The linear relationship between the stress and birefringence tensors is fairly shown to be valid up to intermediate flow strengths (i.e., Wi_d = 91.4 and Wi_R = 22.9), showing consistent behaviors with previous study for the same $C_{400}H_{802}$ PE system under steady shear flow.[23] Also, the stress-optical coefficient C calculated from the data in Figure 4.2.2 (using $\Delta n = C\Delta\sigma$ for the linear part of the n_{xy} vs. σ_{xy} plot) is 1.13 ± 0.52 × 10^{-9} Pa^{-1}, showing a good agreement with previously obtained value under steady shear.[23] Following a further increase in the flow strength [i.e., Wi_d = 371 (Wi_R = 229) and Wi_d = 928 (Wi_R = 229)], not only the plot exhibits a nonlinear trend, also the values of n_{xy} at a given σ_{xy} also appear to be different from the corresponding ones at lower flow strengths.

Additionally, we compare the transient behavior of σ_{xy}, n_{xy}, S_{xy}, $S_{xy}^{ee} = \langle u_{ee,x} u_{ee,y} \rangle$ (where $\mathbf{u}_{ee}$ is the unit chain end-to-end vector), and primitive path L_{pp} as a function of strain in Figure 4.2.2. At relatively low strain rates (Wi_d = 18.6 and Wi_R = 4.57), the σ_{xy}, n_{xy}, and S_{xy} curves appear to overlap, which is considered to linear relationships between these properties. Furthermore, the plot of the orientation tensor S_{xy}^{ee} [representing the largest length scale of chain structure (i.e., the chain end-to-end vector)], quantitatively matches the stress and birefringence curves. In contrast, L_{pp} does not describe the transient overshoot behavior exhibited by the other properties. At stronger flow fields [i.e., Wi_d = 92.8 (Wi_R = 22.9) and Wi_d = 371 (Wi_R = 91.4)], the n_{xy} values for a given σ_{xy} appear to be systematically underestimated as compared to the corresponding values at lower flow strengths, corresponding to the breakdown of the SOR. However, it is important to notice that the overall evolution (i.e., uphill, maximum, and downhill) of the birefringence as a function of strain coincides exactly with that of the stress. On the other hand, S_{xy}^{ee} displays a trend of overestimation relative to that of the stress, indicating that the orientation tensor based on the largest structural length scales is less capable of representing the stress response. Interestingly, the S_{xy} curve calculated from the entanglement strands turn out to match the σ_{xy} one even at rather high flow strengths. This result would support the use of the entanglement strand as a fundamental length unit in modeling entangled polymeric systems. In sharp contrast with this finding, however, the figure also shows that the plot of L_{pp} does not properly reflect the stress response. At very high flow fields (i.e., Wi_d = 928 and Wi_R = 229), some quantitative differences emerge between the S_{xy} and σ_{xy} curves; however, the S_{xy} data still provide the best representation of the stress response of the system, among all the structural measures examined.

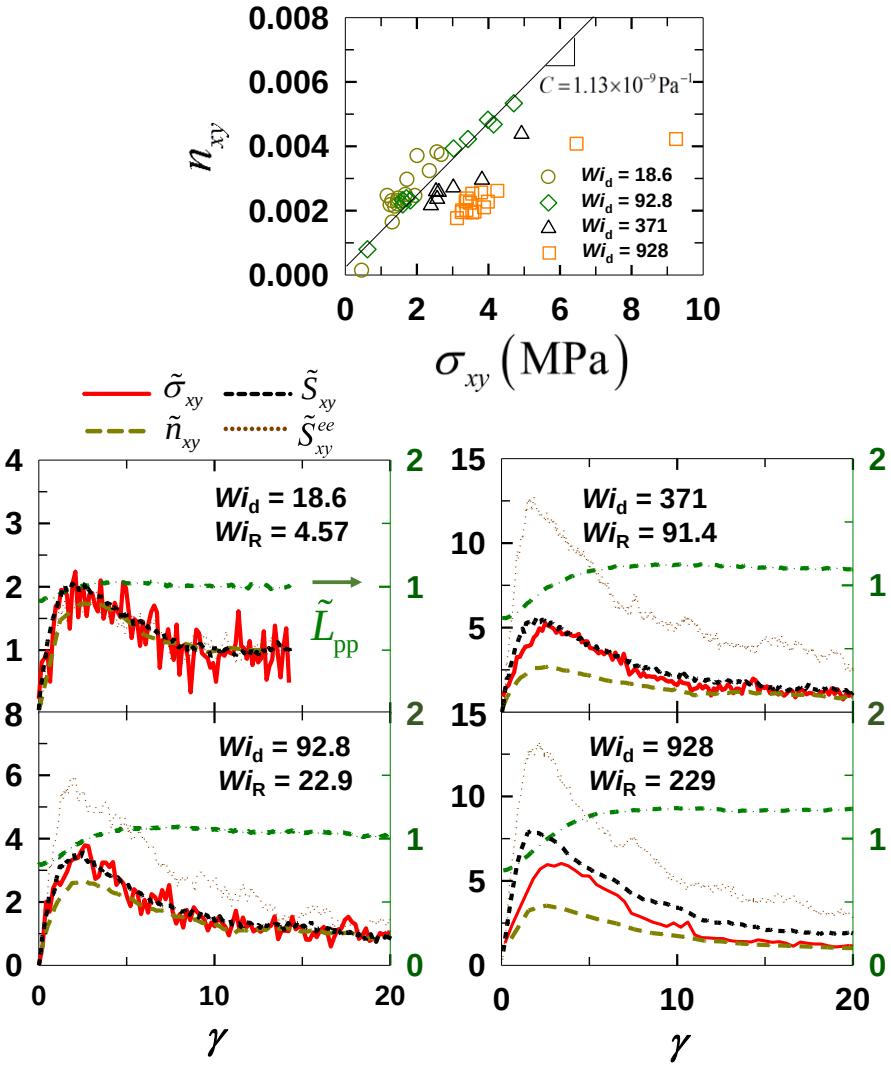

Figure 4.2.2 (Top) Plot of birefringence n_{xy} versus shear stress σ_{xy} at four different flow strengths: $Wi_d = 18.6$ and $Wi_R = 4.57$ (dark yellow circles), $Wi_d = 92.8$ and $Wi_R = 22.9$ (dark green diamonds), $Wi_d = 371$ and $Wi_R = 91.4$ (black triangles), and $Wi_d = 928$ and $Wi_R = 229$ (orange squares). (Bottom) Plots of σ_{xy} (red solid lines), n_{xy} (dark yellow long-dashed lines), S_{xy} (eq. 4.2.1, black short-dashed lines), and $S^{ee}_{xy} = \langle u_{ee,x} u_{ee,y} \rangle$ (dark brown dotted lines, where $\mathbf{u}_{ee}$ is the unit chain end-to-end vector), as a function of strain for the simulated C_{400} PE melt under start-up shear at four different flow strengths; each property is normalized by its steady-state value. For comparison purposes, the corresponding result of L_{pp} (dark green dashed-dotted lines) is also shown in each plot.

4.2.2 Molecular mechanisms behind the overshoot

We now consider a collective chain orientation to a certain angle with respect to the flow direction that develops during start-up shear, which generates an anisotropic environment for the rotational dynamics of the individual chains. Top panel in Fig. 4.2.3 presents the angular probability distribution function $P(\theta)$ for the chain orientation angle θ with respect to the flow direction as a function of strain. And we also calculated the stress contributed solely by the intermolecular Lennard-Jones (LJ) interaction between chains as a function of strain (middle and bottom panel in Fig. 4.2.3). While the transient behavior of the intermolecular LJ shear stress $\sigma_{xy}^{\text{inter}}$ and normal stress difference N_1^{inter} appears to be qualitatively consistent with that of $P(\theta)$, the exact distributions of $\sigma_{xy}^{\text{inter}}$ and N_1^{inter} with respect to θ and γ are somewhat different from each other. It is particularly important to notice in the result that $\sigma_{xy}^{\text{inter}}$ exhibits a maximum for $\theta \approx 20°$ at the peak strain $\gamma_{\sigma\text{m}} = 2.5$ for shear stress. A polymer molecule will experience a large frictional drag (via intermolecular interactions with surrounding chains) for execution of overall rotation, if it is surrounded by neighboring chains that are collectively oriented at a certain angle. Thus, the degree of intermolecular collisions between chains is strongest in the vicinity of $\theta = 20°$; this implies the existence of "collisional" angular regimes near this critical angle in the transient polymer rotational dynamics (Fig. 4.2.4). This microscopic characteristic is considered to eventually lead to the shear stress overshoot at the corresponding peak strain (a detailed analysis will be presented later). By comparison, the first normal stress difference N_1^{inter} contributed by the intermolecular LJ interaction exhibits a maximum peak around θ = 10° at $\gamma = 5$ (approximately twice that of shear stress) (bottom panel in Fig. 4.2.3).

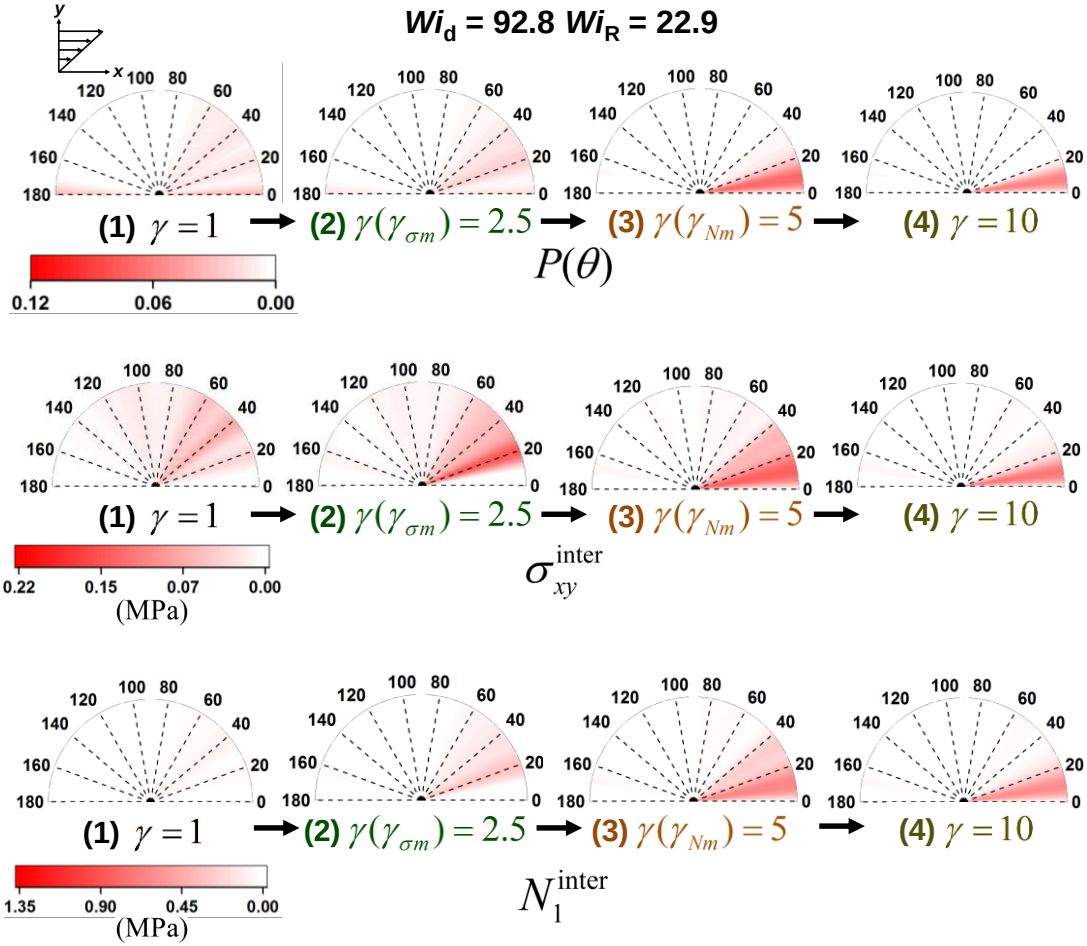

Figure 4.2.3. (Top) Angular probability distribution function $P(\theta)$ for the chain orientation angle θ. Here, θ was computed based on the chain center-to-center vector (connecting two centers of mass of the bisected chain), which was shown to more precisely describe the rotational dynamics of individual chains in comparison with the chain end-to-end vector. (Bottom) Distribution of shear stress σ_{xy}^{inter} and the first normal stress difference N_1^{inter} contributed solely by the intermolecular LJ interactions between chains with respect to θ as a function of strain.

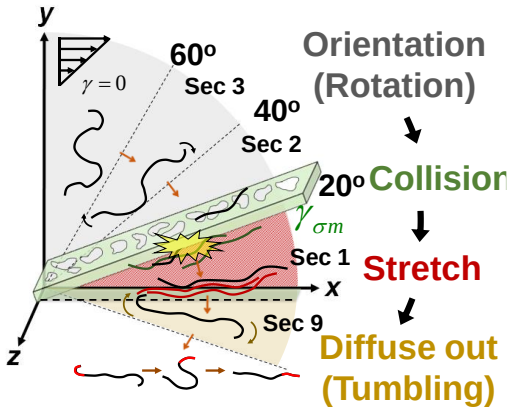

Figure 4.2.4. Schematic illustration of the overall characteristic molecular mechanisms of polymer chains associated with the stress overshoot phenomena upon exposure to the flow field.

Based on this orientational inhomogeneity of the shear and normal stress of the system before reaching a steady-state under start-up shear, we carried out a detailed analysis of the structural and rheological properties for each specific angular region (a total of nine Sections between θ=0° and 180°, each spanning 20°). Note that the transient behavior of the shear stress is mainly governed by the intermolecular LJ interaction (i.e., $\sigma_{xy}^{\text{inter}}$) at the Sec 2 angular region (20° ≤ θ ≤ 40°) for all *Wi* numbers studied here (Fig. 4.2.5); i.e., the σ_{xy} overshoot is consistent with that of $\sigma_{xy}^{\text{inter}}$. Thus, it can be thought that the transient nonlinear behaviors of shear stress for polymeric systems under shear are essentially associated with the chains belonging to the angular region of Sec 2, irrespective of the imposed flow strength. Further analysis reveals that the polymer chains of Sec 2 begin to enter the angular region of Sec 1 (0° ≤ θ ≤ 20°) at approximately θ = 20° (collisional angular regime) where a relatively large number of chains are collectively oriented (top panel in Fig. 4.2.3). Therefore, the polymer chains belonging to Sec 2 undergoe strong intermolecular collisions with the chains in the collision regime, which finally induces the shear stress overshoot at the corresponding strain. In order to understand this collisional angular regime, we computed the angular velocity of the chain rotation directly, by tracking the individual chain motion before stress overshoot. The average angular velocities for the clockwise and counterclockwise chain rotations appear to be almost identical in the vicinity of θ = 20° (Fig. 4.2.6). That is, when approaching θ = 20°, the degree of flow-induced convective chain rotation becomes so low as to be comparable to that of the thermally-induced diffusive chain rotation.[30,31] In short, during start-up shear flow, many chains initially rotate towards Sec 2. Then, when they reach an angular regime close to θ = 20°, their rotational advection due to the vorticity field of flow becomes almost sluggish, and chains begin to accumulate in the angular regime, eventually building a collision regime.

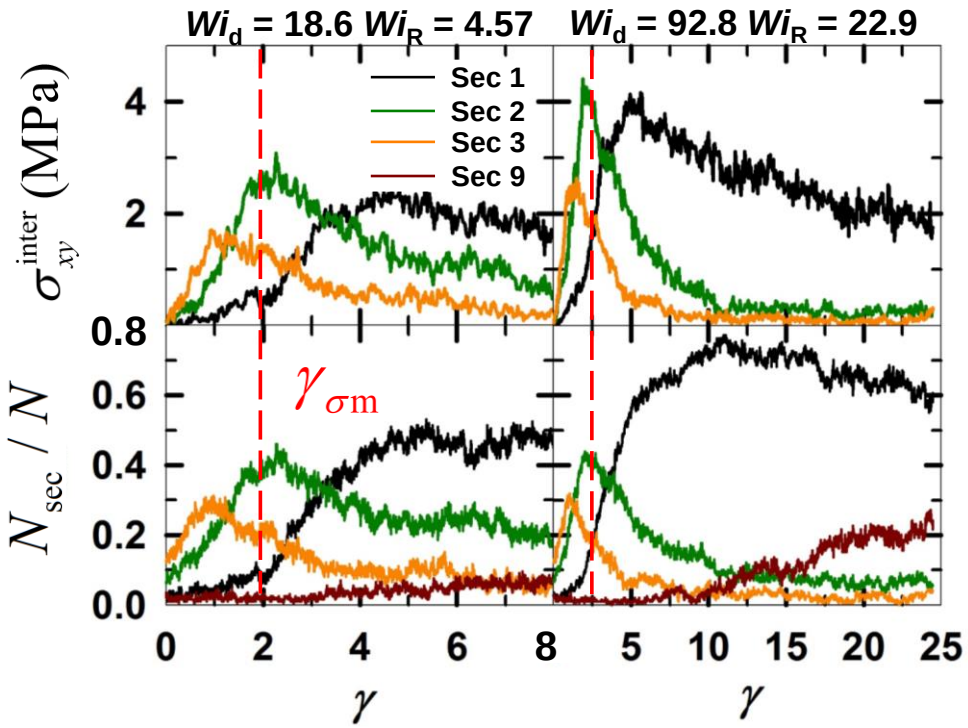

Figure 4.2.5. The number N_{sec} of chains belonging to each angular section (normalized by the total number N of chains) and the corresponding intermolecular LJ shear stress σ_{xy}^{inter} as a function of strain (Sec 1 is specified as $0° \le \theta \le 20°$, Sec 2 as $20° \le \theta \le 40°$, Sec 3 as $40° \le \theta \le 60°$, and Sec 9 as $160° \le \theta \le 180°$).

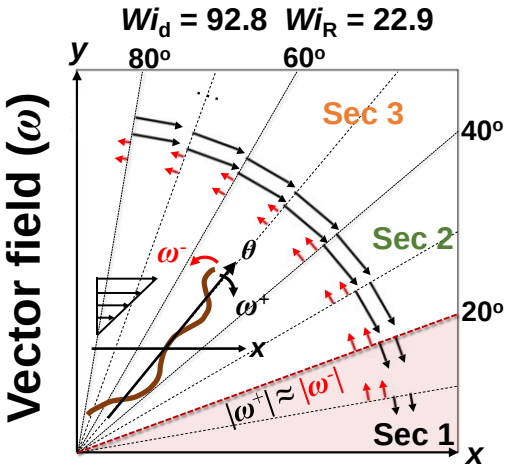

Figure 4.2.6. Vector field of the average angular velocity for clockwise (ω^+, black arrows) and counterclockwise (ω^-, red arrows) chain rotation at each orientation angle before stress overshoot.

After passing through the collision regime (i.e., $\gamma > \gamma_{\sigma m}$), the degree of intermolecular collision between chains (and thus the intermolecular LJ shear stress) decreases rapidly, and the chains begin to stretch with a rather sluggish rotational motion. This chain stretching results in growth of the normal stress difference, eventually leading to an overshoot behavior of N_1 (Fig. 4.2.7). At higher strains, the chains can move out of Sec 1 and enter Sec 9 primarily via random Brownian fluctuations,[30-32] thus a tumbling process is initiated. As shown in Fig. 4.2.7, the plot of $\left\langle R_{ete}^2 \right\rangle$ as a function of strain displays a large variation, which is approximately equivalent to that for the maximum of N_1^{inter} at the corresponding strain. It is therefore asserted that the normal stress overshoot is closely connected with the global chain stretch in addition to the chain orientation. We additionally state that the first normal stress difference exhibits an overshoot at a strain value where $\left\langle R_{ete}^2 \right\rangle$ crosses its steady-state value during the initial growth stage. Although seemingly fortuitous, this result can support physical aspect of the normal stress overshoot being associated with the overall chain stretch.

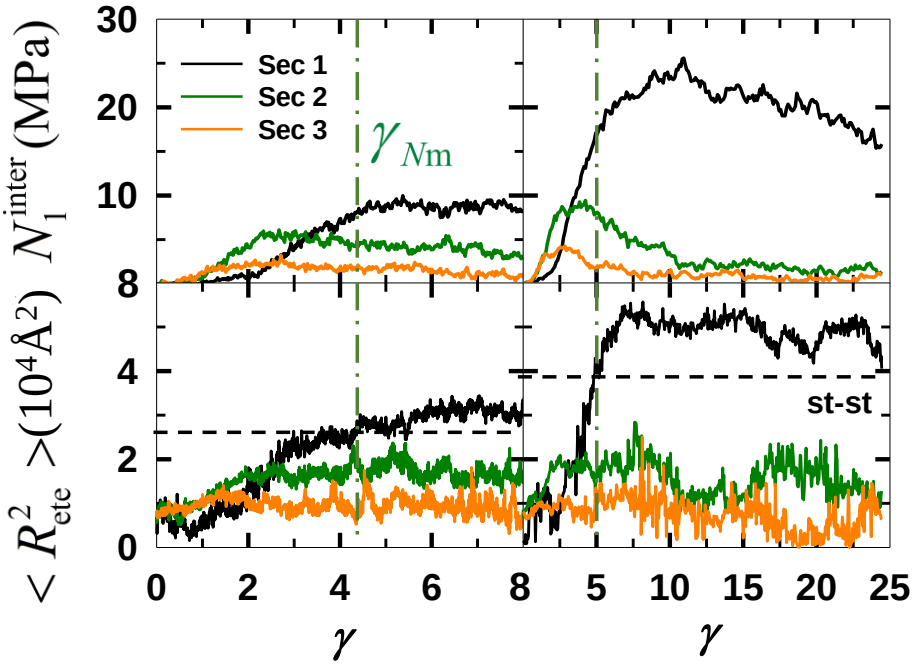

Figure 4.2.7. The first normal stress difference N_1^{inter} of intermolecular LJ interaction and the mean-square chain end-to-end distance $\left\langle R^2_{ete} \right\rangle$ for each angular section as a function of strain.

In this work, we investigated the intrinsic rheological characteristics underlying the stress overshoot for entangled polymer systems under start-up shear flow through a molecular-level analysis of transient chain dynamics using atomistic NEMD simulations. It is found that detailed knowledge of the temporal evolution of the chain orientational anisotropy is the key to understanding the fundamental physics behind the stress overshoot phenomena. That is, as applied the imposed flow field, the polymer chains undergo the highest degree of intermolecular collision between polymer chains in the collisional angular regime in the vicinity of θ=15°–25° (corresponding to $\gamma_{\sigma m} = 2-4$) where a large number of chains are concertedly oriented in association with the counterbalance between the flow-induced and the thermally-induced (diffusive) chain rotations. Accordingly, the overall transient (increasing to a maximum and then decreasing) behavior of shear stress can be adequately described by the temporal variation of intermolecular LJ stress for chains belonging to the angular regime of Sec 2.

4.3 Stress relaxation upon cessation of steady shear flow

Stress relaxation behaviors have been widely utilized in the field of polymer rheology for characterization of material properties and for theoretical development of general constitutive models. However, detailed molecular processes underlying the stress relaxation of polymeric materials remain unknown. Thus, in this study, a thorough analysis of the relaxation behaviors was carried out via direct atomistic NEMD simulations of $C_{400}H_{802}$ entangled linear PE melts for a wide range of flow strengths, corresponding to the Weissenberg number Wi: $18.6 \le Wi \equiv \tau_d \dot{\gamma} \le 928$ with τ_d = 218 ± 10 ns for the C_{400} PE melt at constant temperature T = 450 K and density ρ = 0.7640 g/cm^3 (corresponding to the pressure P = 1 atm of the simulated system).[23] The corresponding Rouse time of the system was estimated as τ_R = 53.7 ± 10 ns.[21] The NEMD simulations were executed with the well-known p-SLLOD algorithm[6,7] and SKS united-atom potential model,[11] implemented by a Nosé–Hoover thermostat[8,9] and the standard Lees–Edwards sliding-brick boundary conditions[13] using the r-RESPA.[10] This study aims to elucidate the basic molecular characteristics behind the stress relaxation phenomena of entangled linear polymer melts upon cessation of steady shear flow. Here, two separate relaxation mechanisms were identified: fast structural relaxation via the entropic chain retraction force and the induced orientational relaxation, and slow thermally-driven orientational relaxation. We directly confirmed these processes, and also demonstrated the physical origins for several well-known experimental observations of stress relaxation behaviors.

4.3.1 Stress relaxation

As imposed flow field is off, polymeric system begins to experience relaxational process to reach the equilibrium state. First, we plot transient behaviors of the stress tensors and chain structure with orientation in Figure 4.3.1. Left panel in Fig. 4.3.1 shows transient relaxation behaviors of shear stress (σ_{xy}) and the first normal stress difference ($N_1 \equiv \sigma_{xx} - \sigma_{yy}$) of the simulated C_{400} PE melt system as a function of time upon cessation of steady shear flow at three different *Wi* numbers. As generally revealed in reported experiments,[1,49,50] both σ_{xy} and N_1 exhibit a faster relaxation with increasing *Wi* number, and σ_{xy} relaxes faster than N_1 at a given *Wi* number. The transient behaviors of σ_{xy} and N_1 are well-characterized by the birefringence tensor (also satisfying the well-known stress-optical rule)[15,21] and the order tensor of entanglement strands along the chain in association with the tube theory of polymer melt systems. Here, $\mathbf{S}$ is defined as $S_{\alpha\beta} = \frac{1}{N_{seg}} \sum_{i=1}^{N_{seg}} \left\langle \frac{(r_{i+1} - r_i)_\alpha (r_{i+1} - r_i)_\beta}{(\mathbf{r}_{i+1} - \mathbf{r}_i)^2} \right\rangle$ where $\mathbf{r}_i$ denotes the end-to-end vector of the i^{th} entanglement strand, and N_{seg} is the total number of entanglement strands, based on the number N_e of carbon atoms per entanglement strand (N_e = 68 for polyethylene[29]). As shown in previous theoretical and experimental analyses,[1,21,51] the stress tensor of polymeric systems can be successfully in line with the chain end-to-end vector **R** (or the entanglement strand vector). In right panel in Fig. 4.3.1, the transient behaviors of stress are directly compared with those of the average chain orientation angle θ and chain end-to-end distance $|\mathbf{R}|$. Note that each property is normalized (as indicated by the tilde symbol) as $\frac{\langle A \rangle - \langle A \rangle_{eq}}{\langle A \rangle_{st-st} - \langle A \rangle_{eq}}$ where $\langle A \rangle_{eq}$ and $\langle A \rangle_{st-st}$ are the equilibrium and steady-state values of a property *A*, respectively. Clearly, the stress relaxation does not exactly match the relaxations of either θ or $|\mathbf{R}|$. Also, the θ-relaxation appears to be slowest among them at all *Wi* numbers. Moreover, N_1 is quite well described by the $|\mathbf{R}|$-relaxation (except for a small deviation), supporting a common theoretical knowledge on the close relationship between N_1 and $|\mathbf{R}|$ that already reported by various experimental and numerical studies.[1,51-53] Importantly, the faster relaxation at the higher flow strength is accurately observed in all the quantities.

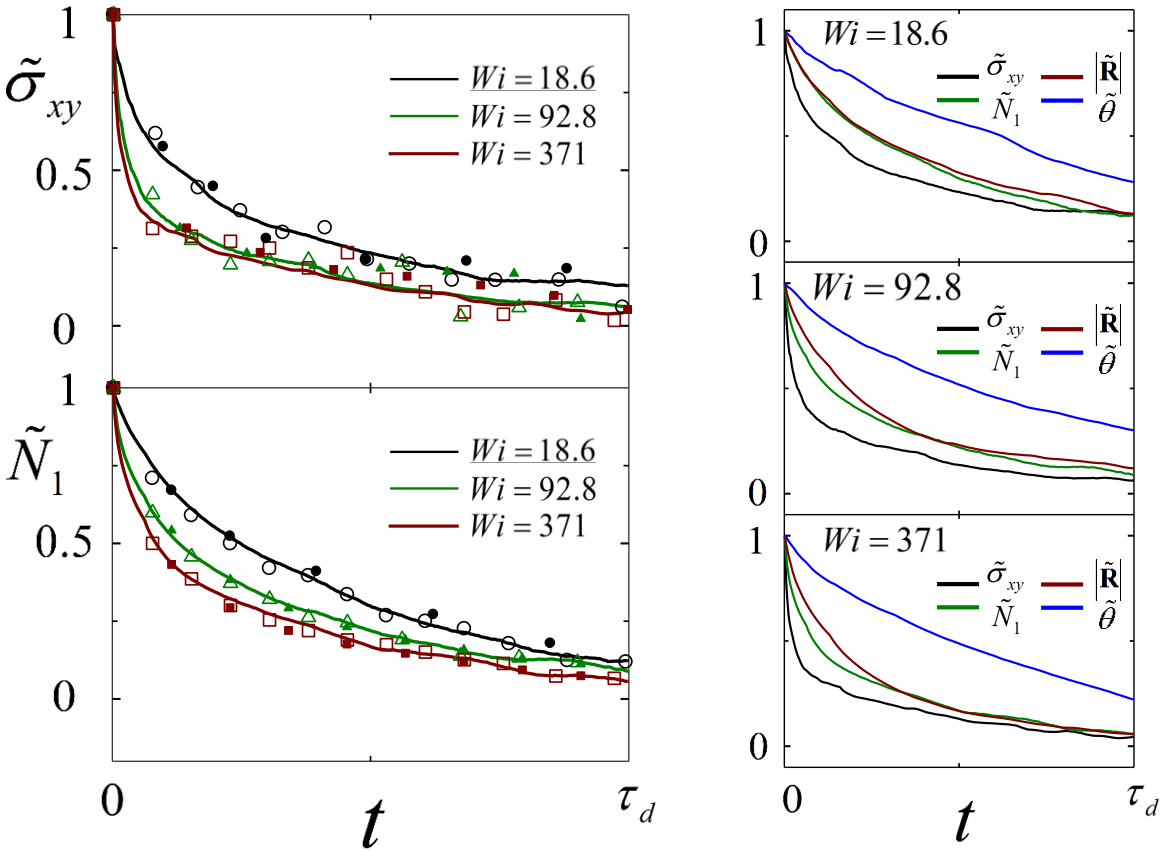

Figure 4.3.1 (Left) Transient behaviors of stress and chain structure. Relaxation behaviors of shear stress σ_{xy} (upper panel) and the first normal stress difference $N_1(\equiv \sigma_{xx} - \sigma_{yy})$ (bottom panel) for three different *Wi* numbers. The empty and filled symbols represent the corresponding (*xy* or *xx*–*yy*) component of the birefringence tensor $\mathbf{n}$ and the orientation tensor $\mathbf{S}$ of entanglement strands, respectively. (Right) Comparison of the transient behaviors of stress with those of the chain end-to-end distance $|\mathbf{R}|$ and orientation angle θ (the angle between the flow (*x*-)direction and the director which is the eigenvector corresponding to the largest eigenvalue of the order tensor based on the chain end-to-end vector).

Then, a fundamental question is raised here: how does the stress of polymer system imposed by an external flow field relax upon cessation of the flow? Undergoing shear flow, chains tend to show largely deformed structure (i.e., $|\mathbf{R}| > |\mathbf{R}|_{eq}$). As is well known, the stretched chain conformation would induce an entropically-driven chain retraction force, which effectively balances against the chain-stretching force imposed by the external flow at steady states. Thus, after switching off the flow, the retraction force relaxes the chains to recover the original equilibrium conformations, i.e., conformational (or structural) relaxation as $\frac{d|\mathbf{R}|}{dt} < 0$. Moreover, the structural relaxation concurrently induces the orientational relaxation (i.e., $\frac{d\theta}{dt} > 0$), leading to no preference for the flow direction by the steady-state shear flow. Consequently, the structural and induced orientational relaxations together are considered to affect the overall relaxation. this induced orientational relaxation particularly facilitates the spatial decorrelation between the *x*- and *y*-directions of the chain orientation, leading to a further reduction for σ_{xy} in comparison with N_1. Meanwhile, in addition to the flow-associated structural and induced orientational relaxations, a thermally-driven orientational relaxation independent of the flow field would make the system attain the original spatial homogeneity and isotropicity of the equilibrium state (i.e., $\sigma_{xy} = N_1 = 0$).

Based on this concept, we can readily understand why σ_{xy} and N_1 relax faster as the flow strength increases. With increasing flow field, chains tend to become more stretched and aligned in the flow direction. A higher chain stretch would give rise to the larger chain retraction force, thereby increasing the structural relaxation rate (i.e., $\frac{d|\mathbf{R}|}{dt}$), finally inducing a higher orientational relaxation as well. Thus, the structural and induced orientational relaxation rates would be accelerated as *Wi* increases, thereby enhancing the stress relaxation. This can be confirmed in $\frac{d|\mathbf{R}|}{dt}$ and $\frac{d\theta}{dt}$ from the NEMD simulations (Fig. 4.3.2). Moreover, in view of individual chain dynamics, a main contribution to the overall magnitude of $\frac{d|\mathbf{R}|}{dt}$ (and the induced $\frac{d\theta}{dt}$) would be dominated by the highly stretched chains with large values of $|\mathbf{R}|$ (having a large chain retraction force). Because the number of chains for large $|\mathbf{R}|$ generally increases with increasing applied shear, the contribution of the stretched chains to the overall structural and induced orientational relaxations would become larger with increasing *Wi* number, thereby facilitating the stress relaxation. This feature is clearly verified in Fig. 4.3.3. Additionally, note that a higher degree of chain alignment at a larger flow strength effectively decreases the translational

hydrodynamic friction of chain motion parallel to the aligned direction, promoting the structural and induced orientational relaxation.

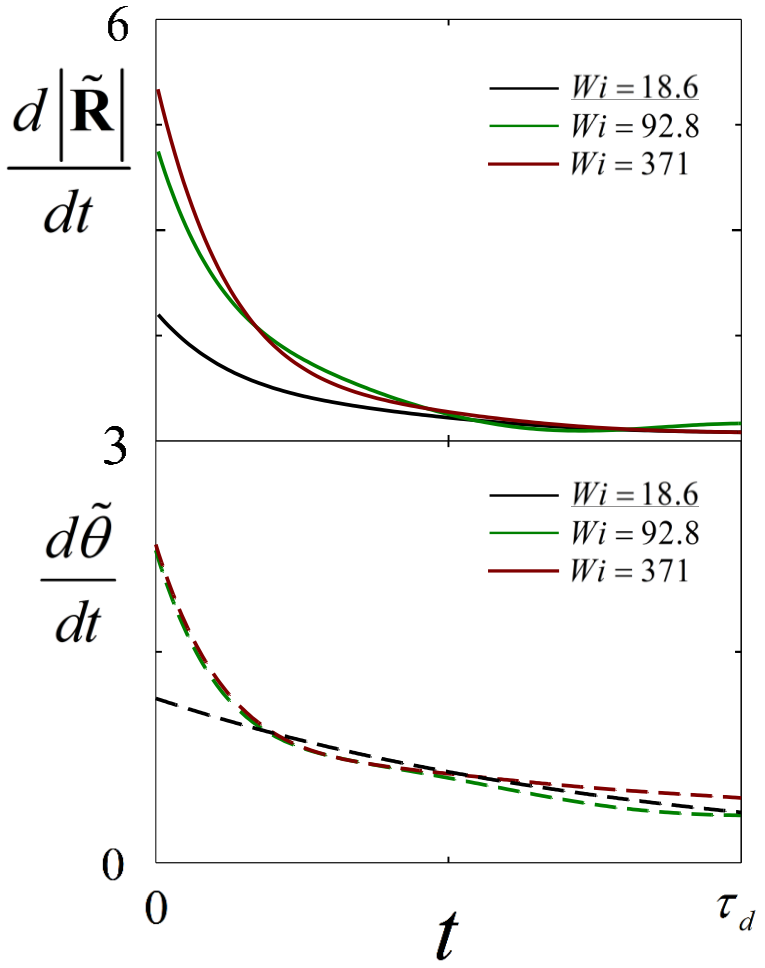

Figure 4.3.2 Structural and orientational relaxation rates. Magnitude of structural relaxation rate $\frac{d|\tilde{\mathbf{R}}|}{dt}$ (upper panel) and orientational relaxation rate $\frac{d\tilde{\theta}}{dt}$ (bottom panel), evaluated by using an 8th-order polynomial fit of $|\tilde{\mathbf{R}}|$ and $\tilde{\theta}$, for different *Wi* numbers.

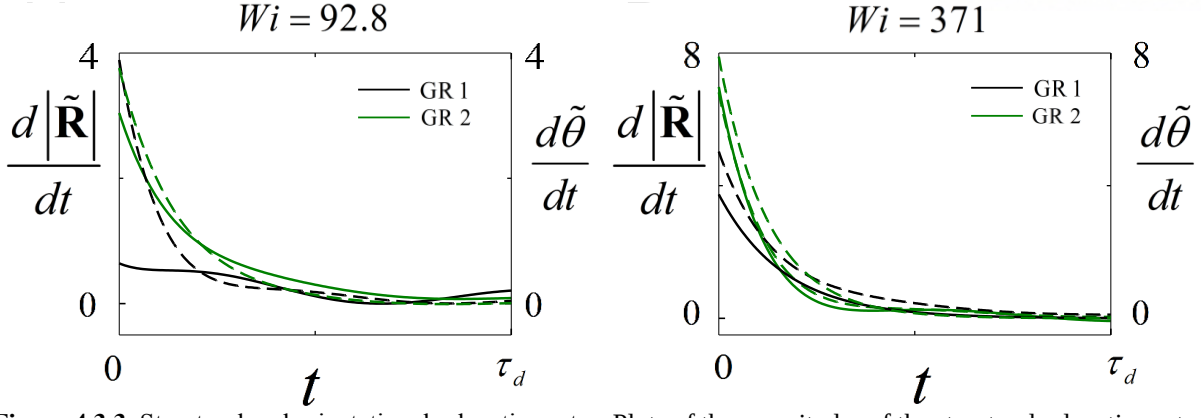

Figure 4.3.3. Structural and orientational relaxation rates. Plots of the magnitudes of the structural relaxation rate $\frac{d|\mathbf{R}|}{dt}$ (solid lines) and the orientational relaxation rate $\frac{d\theta}{dt}$ (dashed lines) for each group of the steady-state chain end-to-end distance $|\mathbf{R}_{st-st}|$ relative to the equilibrium one $\langle|\mathbf{R}_{eq}|\rangle$ as a function of time for (Left) *Wi*=92.8 and (Right) *Wi*=371. Here, GR 1 is specified as $\langle|\mathbf{R}_{eq}|\rangle < |\mathbf{R}_{st-st}| \le 2\langle|\mathbf{R}_{eq}|\rangle$ and GR 2 as $2\langle|\mathbf{R}_{eq}|\rangle < |\mathbf{R}_{st-st}|$. $\langle|\mathbf{R}_{eq}|\rangle$ = 89.52±14.14 Å for the simulated $C_{400}H_{802}$ PE melt. Note that each property is normalized (as indicated by the tilde symbol) as $\frac{\langle A\rangle - \langle A\rangle_{eq}}{\langle A\rangle_{st-st} - \langle A\rangle_{eq}}$ where $\langle A\rangle_{eq}$ and $\langle A\rangle_{st-st}$ are the equilibrium and steady-state values of a property *A*, respectively.

We then consider why the relaxation of σ_{xy} is generally faster than that of N_1 at a given shear rate. It is noted that N_1, by definition, becomes zero only when σ_{xx} is equal to σ_{yy} (similarly for the second normal stress difference $N_2 \equiv \sigma_{yy} - \sigma_{zz}$). Physically, this requires the homogeneity and isotropicity of the whole system with complete structural and orientational relaxations of all chains (i.e., $\langle R^2 \rangle = \langle R^2 \rangle_{eq}$ and $\langle u_x^2 \rangle = \langle u_y^2 \rangle = \langle u_z^2 \rangle = \frac{1}{3}$ for the unit chain end-to-end vector **u**). However, the magnitude of σ_{xy} is likely to decrease due to the orientational decorrelation of chains. For instance, the degree of *xy*-correlation of chain orientation can be approximately estimated in terms of $C_{xy} \equiv \langle u_x u_y \rangle - \langle u_x \rangle \langle u_y \rangle$. Figure 4.3.4 shows the value of C_{xy} as a function of time. Clearly, the degree of *xy*-correlation has become significantly weak at time ($t \simeq \tau_R$), even long before the system acquires the spatial homogeneity and isotropicity at time ($t \simeq \tau_d$), i.e., $\langle u_x^2 \rangle = \langle u_y^2 \rangle$. It is conjectured that a similar tendency would be exhibited by other structural and even dynamical properties.

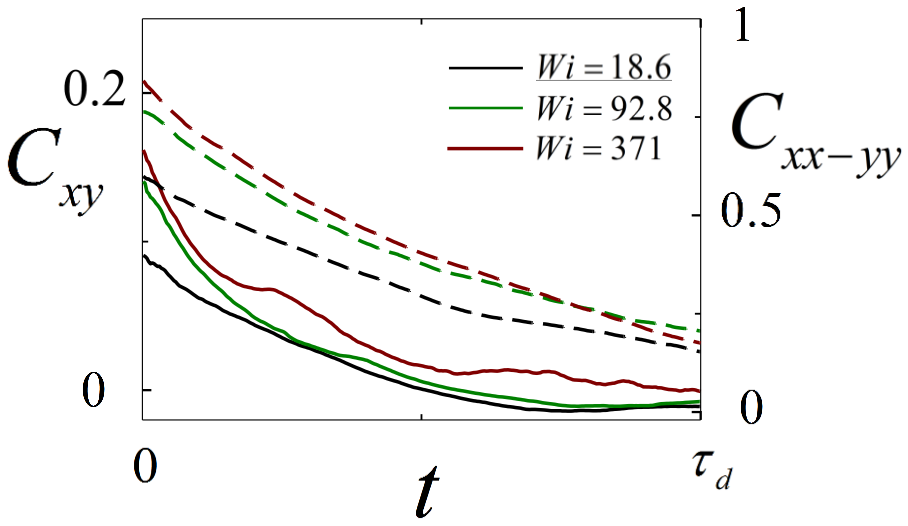

Figure 4.3.4. Relaxation of the correlation functions. Transient behavior of the correlation functions $C_{xy} = \langle u_x u_y \rangle - \langle u_x \rangle \langle u_y \rangle$ (solid lines) and $C_{xx-yy} = \langle u_x^2 \rangle - \langle u_y^2 \rangle$ (dashed lines) of the unit chain end-to-end vector **u** for different *Wi* numbers.

4.3.2 Individual chain analysis

The transient structural behaviors during relaxation were further analyzed based on the mesoscopic brightness method for three distinctive time regimes ($0 < t \le \tau_R$, $\tau_R < t \le 2\tau_R$, and $2\tau_R < t \le \tau_d$) in order to investigate the representative conformational transition of the simulated C_{400} PE melt system. As shown in top panel in Fig. 4.3.5, for $0 < t \le \tau_R$, the end-kink (E-K) conformation is quickly generated during the structural relaxation via the relatively fast motion of chain ends with high free volume in comparison with the rather sluggish chain segments around the backbone center. The maximum distribution of the E-K conformation is observed at $t \simeq \tau_R$. In the meantime, as all chain segments tend to move gradually toward the backbone center via the tensile chain retraction force, the amount of the end-center-kink (E-C-K) conformation also increases. The important feature is a remarkable structural transition from E-K to E-C-K conformation is found to occur for $\tau_R < t \le 2\tau_R$ with the maximum E-C-K distribution at $t \simeq 2\tau_R$ for the simulated C_{400} PE melt. A steady increase of the fold conformation for $0 < t \le 2\tau_R$ via the structural relaxation combined with the induced orientational relaxation occurs also. These conformational transitions in this time period induce a dramatic decrease in the stretched chain conformation. For $2\tau_R < t \le \tau_d$, the conformational transition from the E-C-K and fold to coil appears. Finally, the overall conformational distribution gets closer to the equilibrium one for $t > \tau_d$. These molecular characteristics of the structural relaxation process are schematically summarized in bottom panel in Fig. 4.3.5. Moreover, at $t \simeq 2\tau_R$, where the E-C-K conformation is dominant, the overall chain structure is found to be largely relaxed, thus representing the influential thermally-driven orientational relaxation process with weakened structural and induced orientational relaxation processes. This might indicate there exists such a threshold time regime, which is general to all polymeric systems independent of the applied flow type and strength, and where the structural relaxation becomes nearly complete with exposing a distinctive characteristic of E-C-K chain conformation (see Fig. 4.3.6).

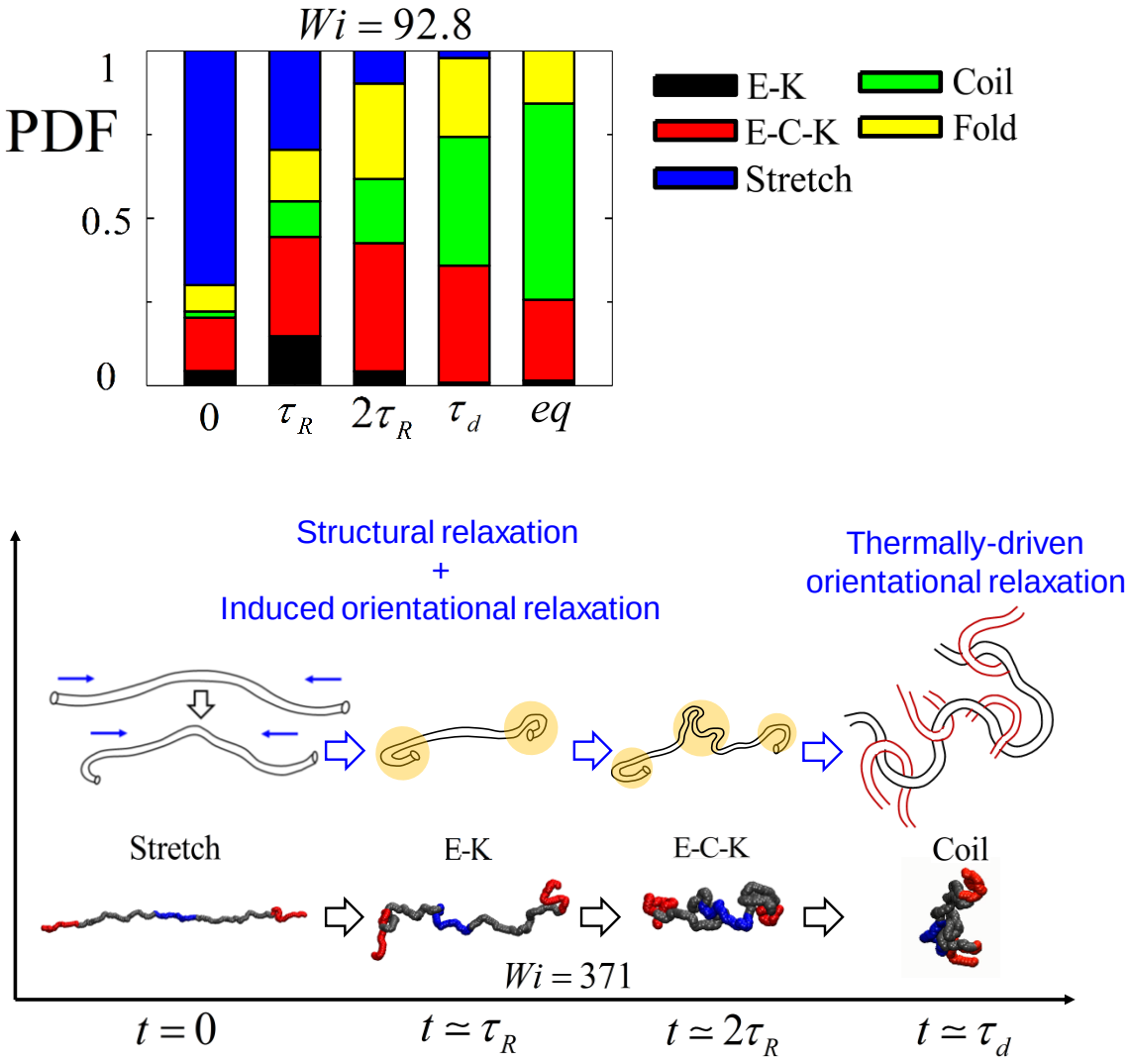

Figure 4.3.5. Structural evolution during relaxation. (Top) Transient behaviors of the probability distribution function (PDF) for the five representative mesoscopic chain configurations [end-kink (E-K), end-center-kink (E-C-K), coil, fold, stretch] computed from the brightness analysis upon cessation of steady shear at $t = 0$. (Bottom) Schematic description of the basic molecular characteristics of structural and orientational relaxation behaviors. Also shown are snapshots of a randomly selected chain at certain specific times during structural relaxation for $Wi = 371$.

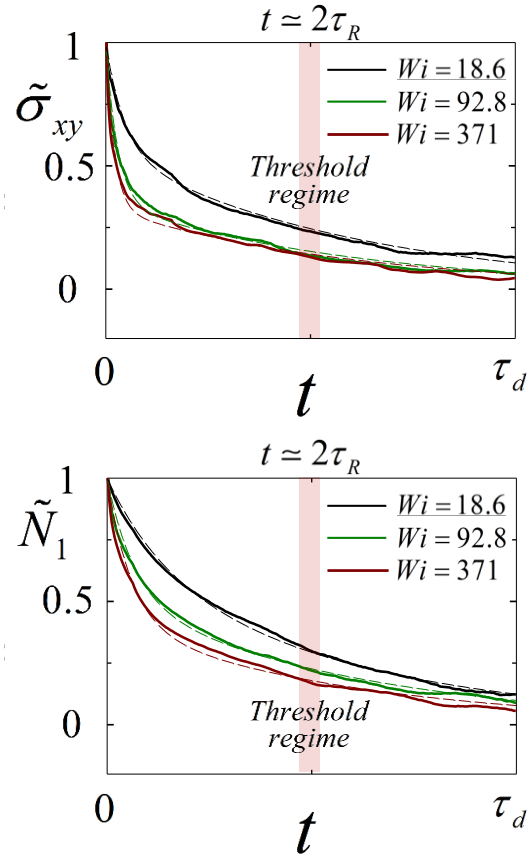

Figure 4.3.6. Transient behaviors of stress and chain structure. Plots of (top) the shear stress σ_{xy} and (bottom) the first normal stress difference N_1 (solid lines) fitted by a simple exponential decay function $\tilde{\sigma}_{xy,xx-yy}(t) = \alpha e^{-t/\tau_1} + (1-\alpha)e^{-t/\tau_2}$ (dashed lines) for three different *Wi* numbers. τ_2 was fixed as equal to $0.7\tau_d$ for all *Wi* numbers. The threshold time regime is marked as red colored area around $t \simeq 2\tau_R$ where the structural and induced orientational relaxations become nearly complete.

4.3.3 Two relaxational processes: structural/orientational and thermally-driven relaxation

In view of the relaxation process involving the initial structural and induced orientational relaxation mechanism and a relatively slower thermally-driven orientational relaxation mechanism (Fig. 4.3.5), we carried out a quantitative analysis for characterizing the overall relaxation behaviors of polymer system based on the following equation $\tilde{\sigma}_{xy,xx-yy}(t) = \alpha e^{-t/\tau_1} + (1-\alpha)e^{-t/\tau_2}$. Here, τ_1 represents a time scale for the fast structural and induced orientational mechanisms and τ_2 that for the slow thermally-driven orientational mechanism. τ_2 is considered to be independent of the flow strength, however, τ_1 is a generally function of the applied flow type and strength, because the probability distribution of $|\mathbf{R}|$ and its average value become different with the flow. This indicates τ_1 would decrease with increasing flow strength because of a larger average chain stretching giving rise to a higher retraction force (also, in addition, an effective decrease of the hydrodynamic friction of chain motion parallel to the aligned direction). Furthermore, the α-value representing the relative contribution to the stress relaxation by the fast structural relaxation is expected to increase with increasing flow strength because the probability distribution of chains with large $|\mathbf{R}|$-values commonly increases with the imposed flow strength (accordingly, α would asymptotically reach a plateau value at very high flow fields, due to saturation of the distribution and average value of $|\mathbf{R}|$). As mentioned earlier, in comparison with N_1, σ_{xy} would relax faster via the structurally-induced orientational relaxation, which promotes the *xy*-decorrelation of chain orientation; thus, τ_1 would be smaller for σ_{xy} than N_1. All these features are clearly evident from the result shown in Fig. 4.3.8 (see also Fig. 4.3.6 and 4.3.7).

As noted above, with increasing shear rate, (i) the average chain retraction force increases due to the increase of $|\mathbf{R}|$, and (ii) the average friction coefficient ξ of chain motion in the aligned direction decreases for the same $|\mathbf{R}|$ due to a highly oriented chains. These two contributions lead to the higher structural and induced orientational relaxation rates for larger *Wi* number. One can approximately extract characteristic information of ξ as a function of *Wi* number using the simulation data of $\langle R^2 \rangle$ vs. *t* based on $\dfrac{\langle R^2 \rangle - \langle R^2 \rangle_{eq}}{\langle R^2 \rangle_{st-st} - \langle R^2 \rangle_{eq}} = \exp\left(-\dfrac{4k}{\xi}t\right) = \exp\left(-\dfrac{t}{\tau}\right)$ with $\tau = \dfrac{\xi}{4k}$, where *k* is the entropic spring constant, e.g., the *k*-value of a finitely extensible nonlinear elastic spring would increase with increasing *Wi* number via an increase of $|\mathbf{R}|$ — see Fig. 4.3.7. The result presented in the bottom panel in Fig. 4.3.8 confirms the decreasing tendency of ξ with increasing flow strength and also shows a consistent scaling behavior between ξ and τ_1. It is noted that ξ would generally not only be a function

of *Wi* number but also a function of time for a given *Wi* number because the overall chain configurations of the system and, thus, the average surrounding environment of individual chains change with time in the course of the relaxation process. Correspondingly, the structural and induced orientational relaxations of a chain of a given $|\mathbf{R}|$-value and its contribution to σ_{xy} and N_1 would vary with *Wi* number because of the alteration of its surrounding environment with the flow strength.

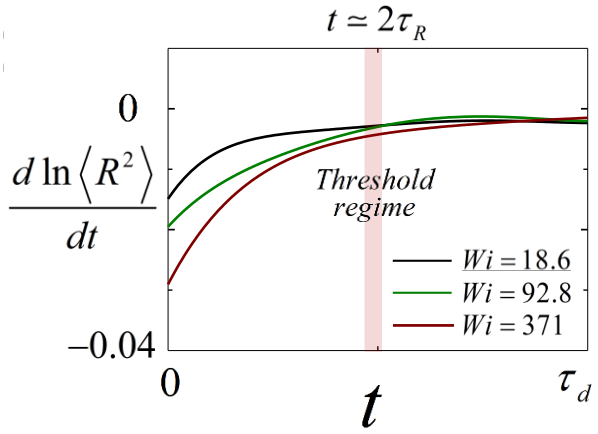

Figure 4.3.7. Plot of $\frac{d \ln \langle R^2 \rangle}{dt} = -\frac{4k}{\xi} = -\frac{1}{\tau}$ vs. time for different *Wi* numbers.

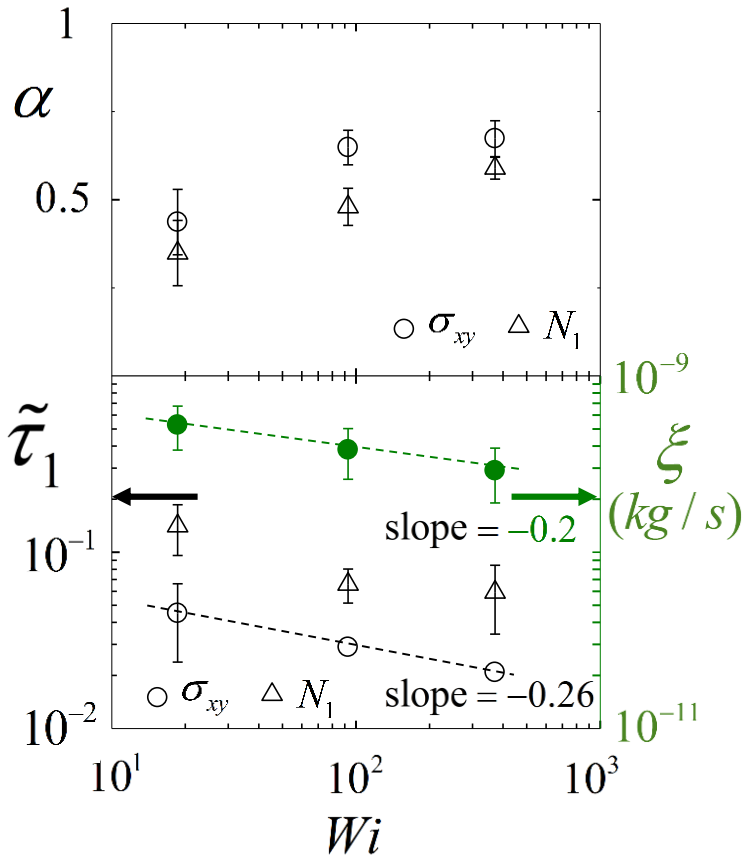

Figure 4.3.8. Plots of the parameters α (upper panel) and $\tilde{\tau}_1 (= \tau_1 / \tau_d)$ (bottom panel) in a simple exponential decay function $\tilde{\sigma}(t) = \alpha e^{-t/\tau_1} + (1-\alpha) e^{-t/\tau_2}$ characterizing the relaxation behaviors of σ_{xy} and N_1 (Fig. 4.3.6) for different *Wi* numbers. Here τ_2 was fixed as equal to $0.7\tau_d$ for all *Wi* numbers. Additionally, the

frictional coefficient ξ (the right y-axis in bottom panel) is calculated based on equation $\frac{\langle R^2 \rangle - \langle R^2 \rangle_{eq}}{\langle R^2 \rangle_{st-st} - \langle R^2 \rangle_{eq}} = \exp\left(-\frac{4k}{\xi}t\right) = \exp\left(-\frac{t}{\tau}\right)$ (Fig. 4.3.7).

Summarizing, the fundamental molecular process behind the stress relaxation behaviors of entangled linear polymer melts upon cessation of steady shear flow has been studied using atomistic NEMD simulations. Two separate relaxation mechanisms were characterized: (i) initial fast structural relaxation (via the entropic retraction force for stretched chains) and the simultaneously induced orientational relaxation, and (ii) relatively slow thermally-driven orientational relaxation. In contrast to the essentially flow-independent nature of mechanism (ii), mechanism (i) is strongly dependent on the imposed flow type and strength because of a large variation of the probability distribution of $|\mathbf{R}|$ (and its average) and the anisotropic hydrodynamic friction of chain motion as a function of the flow field. These basic processes, as confirmed and quantified in this study, support the well-known experimental observations of stress relaxation phenomena of polymer systems. Furthermore, the direct measurement of individual chain dynamics via a brightness analysis of mesoscopic chain structures shows the basic conformational transition of polymer chains during relaxation.

V. CONCLUSION

In conclusion, we successfully have analyzed the intrinsic rheological characteristics underlying the stress overshoot, interfacial chain dynamics, and stress relaxation for polymer melts systems under shear flow, via a detailed molecular-level analysis using direct atomistic NEMD simulations. As polymer systems undergo start-up shear flow, it is demonstrated that orientational inhomogeneity induced by chain orientation (due to imposed flow) underlies the stress overshoot. Also, in the shearing confined linear polymer system, three distinctive characteristic regimes with respective mechanisms are found. Based on this finding, present studies demonstrated effects of short-chain branches and close-loop conformation of polymers on interfacial chain dynamics, in comparison with the linear polymer systems. Additionally, it is also known that the stress relaxation is governed by two mechanisms: (i) initial fast structural relaxation and the simultaneously induced orientational relaxation, and (ii) relatively slow thermally-driven orientational relaxation.

Although specific values of properties would depend on the details of the polymer chemistry or imposed flow strength/type, on the basis of the general features revealed in the present study, it would help us to extend our understanding in the basic characteristics and representative molecular mechanisms and dynamics generally observed in various polymeric systems.

VI. REFENCES

(1) Doi, M.; Edwards, S. F. *The Theory of Polymer Dynamics*; Oxford University Press: New York, 1986.

(2) Lax, M. Fluctuations from the nonequilibrium steady state. *Rev. Mod. Phys.* **1960**, *32*, 25.

(3) Viovy, J. L.; Rubinstein, M.; Colby, R. H. Constraint release in polymer melts: Tube reorganization versus tube dilation. *Macromolecules* **1991**, *24*, 3587-3596.

(4) Milner, S. T.; McLeish, T. C. B. Reptation and contour-length fluctuations in melts of linear polymers. *Phys. Rev. Lett.* **1998**, *81*, 725.

(5) Morrison, F. A. *Understanding Rheology*; Oxford University Press: New York, 2001.

(6) Baig, C.; Edwards, B. J.; Keffer, D. J.; Cochran, H. D. A proper approach for nonequilibrium molecular dynamics simulations of planar elongational flow. *J. Chem. Phys*. **2005**, *122*, 1141037.

(7) Baig, C.; Edwards, B. J.; Keffer, D. J.; Cochran, H. D. Rheological and structural studies of liquid decane, hexadecane, and tetracosane under planar elongational flow using nonequilibrium molecular-dynamics simulations. *J. Chem. Phys.* **2005**, *122*, 184906.

(8) Nosé, S. A molecular dynamics method for simulations in the canonical ensemble. Mol. Phys. **1984**, *52*, 255−268.

(9) Hoover, W. G. Canonical dynamics: Equilibrium phase-space distributions. *Phys. Rev. A: At., Mol., Opt. Phys.* **1985**, *31*, 1695−1697.

(10) Tuckerman, M.; Berne, B. J.; Martyna, G. J. Reversible multiple time scale molecular dynamics. *J. Chem. Phys.* **1992**, *97*, 1990−2001.

(11) Siepmann, J. I.; Karaborni, S.; Smit, B. Simulating the critical properties of complex fluids. *Nature* **1993**, *365*, 330−332.

(12) Martin, M. G.; Siepmann, J. I. Novel Configurational-Bias Monte Carlo Method for Branched Molecules. Transferable Potentials for Phase Equilibria. 2. United-Atom Description of Branched Alkanes. *J. Phys. Chem. B* **1999**, *103*, 4508−4517.

(13) Evans, D. J.; Morriss, G. P. *Statistical Mechanics of Nonequilibrium Liquids*; Academic Press: New York, 1990.

(14) Janeschitz-Kriegl, H. *Polymer Melt Rheology and Flow Birefringence*; Springer-Verlag: New York, 1983.

(15) Baig, C.; Edwards, B. J.; Keffer, D. J. A molecular dynamics study of the stress-optical behavior of a linear short-chain polyethylene melt under shear. *Rheol. Acta* **2007**, *46*, 1171−1186.

(16) Baig, C. Torsional Linearity in Nonlinear Stress-Optical Regimes for Polymeric Materials. *ACS Macro Lett.* **2016**, *5*, 273−277.

(17) Menezes, E. V.; Graessley, W. W. Nonlinear rheological behavior of polymer systems for several shear-flow histories. *J. Polym. Sci., Part B: Polym. Phys.* **1982**, *20*, 1817-1833.

(18) Pearson, D. S.; Kiss, A. D.; Fetters, L. J.; Doi, M. Flow-Induced Birefringence of Concentrated Polyisoprene Solutions. *J. Rheol.* **1989**, *33*, 517−535.

(19) Graham, R. S.; Likhtman, A. E.; McLeish, T. C. B. Microscopic theory of linear, entangled polymer chains under rapid deformation including chain stretch and convective constraint release. *J. Rheol.* **2003**, *47*, 1171-1200.

(20) Pearson, D. S.; Herbolzheimer, E.; Grizzuti, N.; Marrucci, G. Transient behavior of entangled polymers at high shear rates. *J. Polym. Sci.: Part B* **1991**, *29*, 1589-1597.

(21) Jeong, S; Kim, J. M.; Baig, C. Effect of chain orientation and stretch on the stress overshoot of entangled polymeric materials under start-up shear, *Macromolecules* **2017,** *50*, 3424-3429.

(22) Jeong, S; Kim, J. M.; Baig, C. Molecular characteristics of stress overshoot for polymer melts under start-up shear flow, *J. Chem. Phys.* **2017,** *147*, 234901.

(23) Baig, C.; Mavrantzas, V. G.; Kröger, M. Flow Effects on Melt Structure and Entanglement Network of Linear Polymers: Results from a Nonequilibrium Molecular Dynamics Simulation Study of a Polyethylene Melt in Steady Shear. *Macromolecules* **2010**, *43*, 6886− 6902.

(24) Masubuchi, Y.; Watanabe, H. Origin of stress overshoot under start-up shear in primitive chain network simulation. *ACS Macro Lett.* **2014**, *3*, 1183−1186.

(25) Cao, J.; Likhtman, A. E. Simulating startup shear of entangled polymer melts. *ACS Macro Lett.* **2015**, *4*, 1376−1381.

(26) Mohagheghi, M.; Khomami, B. Molecularly based criteria for shear banding in transient flow of entangled polymeric fluids. *Phys. Rev. E: Stat. Phys., Plasmas, Fluids, Relat. Interdiscip. Top.* **2016**, *93*, 062606.

(27) Kröger, M. Shortest multiple disconnected path for the analysis of entanglements in two-and three-dimensional polymeric systems. *Comput. Phys. Commun.* **2005**, *168*, 209−232.

(28) Jeong, S. H.; Kim, J. M.; Yoon, J.; Tzoumanekas, C.; Kröger, M.; Baig, C. Influence of molecular architecture on the entanglement network: topological analysis of linear, long- and short-chain branched polyethylene melts via Monte Carlo simulations. *Soft Matter* **2016**, *12*, 3770−3786.

(29) Fetters, L. J.; Lohse, D. J.; Milner, S. T.; Graessley, W. W. Packing length influence in linear polymer melts on the entanglement, critical, and reputation molecular weights. *Macromolecules* **1999**, *32*, 6847−6851.

(30) Dalal, I. S.; Hoda, N.; Larson, R. G.; Multiple regimes of deformation in shearing flow of isolated polymers. *J. Rheol.* **2012**, *56*, 305-332.

(31) Hur, J. S.; Shaqfeh, E. S. G.; Babcock, H. P.; Smith, D. E.; Chu, S. Dynamics of dilute and semidilute DNA solutions in the start-up of shear flow. *J. Rheol.* **2001**, *45*, 421-450.

(32) Teixeira, R. E.; Babcock, H. P.; Shaqfeh, E. S. C.; Chu, S. Shear thinning and tumbling dynamics of single polymers in the flow-gradient plane. *Macromolecules* **2005**, *38*, 581-592.

(33) Jeong, S.; Cho, S.; Kim, J. M.; Baig, C. Molecular mechanisms of interfacial slip for polymer melts under shear flow. *J. Rheol.* **2017**, *61*, 253-264.

(34) Jeong, S.; Kim, J. M.; Cho, S.; Baig, C. Effect of short-chain branching on interfacial polymer structure and dynamics under shear flow, *Soft Matter* **2017**,*13*, 8644-8650.

(35) Cui, S. T.; Cummings, P. T.; Cochran, H. D. Molecular simulation of the transition from liquidlike to solidlike behavior in complex fluids confined to nanoscale gaps. *J. Chem. Phys.* **2001**, *114*, 7189−7195.

(36) Venkataramani, V.; Sureshkumar, R.; Khomami, B. Coarse-grained modeling of macromolecular solutions using a configuration-based approach. *J. Rheol.* **2008**, *52*, 1143–1177.

(37) Kim, J. M.; Edwards, B. J.; Keffer D. J.; Khomami, B. Dynamics of individual molecules of linear polyethylene liquids under shear: Atomistic simulation and comparison with a free-draining bead-rod chain. *J. Rheol.* **2010**, *54*, 283–310.

(38) Halverson, J. D.; Lee, W. B.; Grest, G. S.; Grosberg, A. Y.; Kremer, K. Molecular dynamics simulation study of nonconcatenated ring polymers in a melt. I. Statics. *J. Chem. Phys.* **2011**, *134*, 204904.

(39) Brown, S.; Lenczycki, T.; Szamel, G. Influence of topological constraints on the statics and dynamics of ring polymers. *Phys. Rev. E: Stat. Phys., Plasmas, Fluids, Relat. Interdiscip. Top.* **2001**, *63*, 052801.

(40) Kapnistos, M.; Lang, M.; Vlassopoulos, D.; Pyckhout-Hintzen, W.; Richter, D.; Cho, D.; Chang, T.; Rubinstein, M. Unexpected power-law stress relaxation of entangled ring polymers. *Nat. Mater.* **2008**, *7*, 997−1002.

(41) Wittmer, J. P.; Meyer, H.; Johner, A.; Kreer, T.; Baschnagel, J. Algebraic Displacement Correlation in Two-Dimensional Polymer Melts. *Phys. Rev. Lett.* **2010**, *105*, 037802.

(42) Tsolou, G.; Stratikis, N.; Baig, C.; Stephanou, P. S.; Mavrantzas, V. G. Melt Structure and Dynamics of Unentangled Polyethylene Rings: Rouse Theory, Atomistic Molecular Dynamics Simulation, and Comparison with the Linear Analogues. *Macromolecules* **2010**, *43*, 10692−10713.

(43) Hur, K.; Jeong, C.; Winkler, R. G.; Lacevic, N.; Gee, R. H.; Yoon, D. Y. Chain Dynamics of Ring and Linear Polyethylene Melts from Molecular Dynamics Simulations. *Macromolecules* **2011**, *44*, 2311− 2315.

(44) Gooβen, S.; Krutyeva, M.; Sharp, M.; Feoktystov, A.; Allgaier, J.; Pyckhout-Hintzen, W.; Wischnewski, A.; Richter, D. Sensing Polymer Chain Dynamics through Ring Topology: A Neutron Spin Echo Study. *Phys. Rev. Lett.* **2015**, *115*, 148302.

(45) Yoon, J.; Kim, J.; Baig, C. Nonequilibrium molecular dynamics study of ring polymer melts under

shear and elongation flows: A comparison with their linear analogs. *J. Rheol.* **2016**, *60*, 673−685.

(46) Tsalikis, D. G.; Koukoulas, T.; Mavrantzas, V. G.; Pasquino, R.; Vlassopoulos, D.; Pyckhout-Hintzen, W.; Wischnewski, A.; Monkenbusch, M.; Richter, D. Microscopic Structure, Conformation, and Dynamics of Ring and Linear Poly(ethylene oxide) Melts from Detailed Atomistic Molecular Dynamics Simulations: Dependence on Chain Length and Direct Comparison with Experimental Data. *Macromolecules* **2017**, *50*, 2565−2584.

(47) Tsalikis, D. G.; Mavrantzas, V. G.; Vlassopoulos, D. Analysis of Slow Modes in Ring Polymers: Threading of Rings Controls LongTime Relaxation. *ACS Macro Lett.* **2016**, *5*, 755−7604

(48) Jeong, S; Cho, S.; Kim, J. M.; Baig, C. Interfacial molecular structure and dynamics of confined ring polymer melts under shear flow. *Macromolecules* **2018**, *51*, 4670-4677.

(49) Snijkers, F.; Ratkanthwar, K.; Vlassopoulos, D.; Hadjichristidis, N. J. Viscoelasticity, nonlinear shear start-up, and relaxation of entangled star polymers. *Macromolecules* **2013**, *46*, 5702-5713.

(50) Huang, Q.; Costanzo, S.; Das, C.; Vlassopoulos, C. Stress growth and relaxation of dendritically branched macromolecules in shear and uniaxial extension. *J. Rheol.* **2017**, *61*, 35-47.

(51) Bird, R. B.; Armstrong, R. C.; Hassager, O. *Dynamics of Polymeric Liquids. Vol. 1: Fluid Mechanics*; John Wiley and Sons: New York, 1987.

(52) Osaki, K.; Kimura, S.; Kurata, M. Relaxation of shear and normal stresses in step-shear deformation of a polystyrene solution. Comparison with the predictions of the Doi-Edwards theory. *J. Polym. Sci.* **1981**, *19*, 517-527.

(53) Larson, R. G.; Khan, S. A.; Raju, V. R. Relaxation of stress and birefringence in polymers of high molecular weight. *J. Rheol.* **1988**, *32*, 145-161.

ACKNOWLEGMEMENT

This dissertation is based on my researches conducted on 6 years during graduate school in UNIST. I have many friends and colleagues who encouraged me to finish my works. I would like to express my gratitude to all those people.

First of all, I would like to appreciate my advisor, professor Chunggi Baig. He supported me with considerable advice and guidance all the time during my degree. I am sure his effort made me take a step forward to an independent researcher. I appreciate that I was one of his students. I also admire the help of Dr. Jun Mo Kim. I could learn lots of academic things. I was happy to deal with many research topics with them during graduate school.

I am really grateful to my committee members, professor Sang Kyu Kwak, Hyunhub Ko, So Youn Kim, Jiseok Lee, and Han Gi Chae for their expertise, idea and encouragement. Professor Sang Kyu Kwak assisted me for internship application, advice, personal issues, and help regarding computer simulation, even when I was an undergraduate student. Professor Hyunhub Ko and So Youn Kim, who gave lectures during taking my major subjects, they always cheered for me. Also, I have been impressed by assistance of professor Jiseok Lee and Han Gi Chae who responded to my sudden request.

I thank our lab members, Jeongha Yoon, Eun Jung Roh, Miran Ha, Tae Hee Lee, Soowon Cho, Seung Heum Jeong, Jinseong Kim, Uk Jung Kang, Tae Yong Ha, and Dong Yeon Kim for their friendship and support. I am also grateful my friends in UNIST, Se Hun Joo, Insol Hwang, Kyongkwan Ro, Deok Jae Choi, Do Young Kim, Jason Yum, Hung Ho, Yong Han Kim, Dong Yoon Kim, Sang Eon Ham, Sang Hyun Jeong, and others for their unsparing help whenever I was in need.

I am thankful to all members in UNIST dance club union, U-Turn.

Finally, I would like to appreciate my family. They always believed what I did with their full support until finishing my degree.

I have a conviction that my research would not have been conducted well without all.

ACHIEVEMENTS

1. List of publications

(1) Jeong, S.; Cho, S.; Kim, J. M.; Baig, C. Molecular mechanisms of interfacial slip for polymer melts under shear flow, *J. Rheol.* **2017**, *61*, 253-264. [News Mention] & [2017 SPE Korea Award] & [Top 10 Hottest JOR Articles]

(2) Jeong, S.; Kim, J. M.; Baig, C. Effect of chain orientation and stretch on the stress overshoot of entangled polymeric materials under start-up shear, *Macromolecules* **2017,** *50*, 3424-3429.

(3) Cho, S.; Jeong, S.; Kim, J. M.; Baig, C. Molecular dynamics for linear polymer melts in bulk and confined systems under shear flow, *Sci. Rep.* **2017**, *7*, 9004.

(4) Jeong, S.; Kim, J. M.; Cho, S.; Baig, C. Effect of Short-Chain Branching on Interfacial Polymer Structure and Dynamics under Shear Flow, *Soft Matter* **2017**, *13*, 8644-8650.

(5) Jeong, S; Kim, J. M.; Baig, C. Molecular characteristics of stress overshoot for polymer melts under start-up shear flow, *J. Chem. Phys.* **2017,** *147*, 234901.

(6) Jeong, S.; Cho, S.; Kim, J. M.; Baig, C. Interfacial Molecular Structure and Dynamics of Confined Ring Polymer Melts under Shear Flow, *Macromolecules* **2018**, *51*, 4670-4677.

(7) Jeong, S.; Baig, C. Molecular Process of Stress Relaxation for Sheared Polymer Melts, *under Review.*

2. List of presentations (oral/poster) in academic conferences

(1) Jeong, S.; Cho, S.; Kim, J. M.; Baig, C. Mechanism and Dynamics of polymeric melts at Interfaces. 06/2015, 31st International Conference of the Polymer Processing Society, Jeju-island, Korea (**Oral**).

(2) Jeong, S.; Cho, S.; Kim, J. M.; Baig, C. Mechanism of Interfacial Slip for Polymer Melts using Non-equilibrium Molecular Dynamics Simulation. 04/2016, The Korean Institute of Chemical Engineers Spring Symposium, Busan, Korea (**Oral**) [Young Women Researcher Award].

(3) Jeong, S.; Cho, S.; Kim, J. M.; Baig, C. 전단 흐름 아래의 폴리머 멜트에서 계면 슬립 현상의 분자 레벨적인 메커니즘. 05/2016, The Korean Society of Rheology, Seoul, Korea (**Oral**).

(4) Jeong, S.; Kim, J. M.; Baig, C. Startup-shear 에서 고분자 용융체 (Polymer Melts) Stress Overshoot 현상의 해석. 11/2016, The Korean Society of Rheology, Busan, Korea (**Oral**).

(5) Jeong, S.; Cho, S.; Kim, J. M.; Baig, C. 전단 유동 (shear flow) 아래 고분자 용융체 (polymer melts) interfacial slip 의 분자 레벨 메커니즘. 06/2017, SPE Korea, Suwon, Korea (Invited/**Oral**) [2017 SPE Korea Award].

(6) Jeong, S.; Kim, J. M.; Cho, S.; Baig, C. Effect of Short-Chain Branching on Interfacial Polymer Dynamics under Shear Flow. 10/2017, The Korean Institute of Chemical Engineers Fall Symposium, Daejeon, Korea (**Oral**) [Excellent Oral Presentation Award].

(7) Jeong, S.; Kim, J. M.; Cho, S.; Baig, C. 전단 흐름 아래 interfacial ring polymer melts 의 구조 및 동역학적 성질 연구. 11/2017, KSR, Jinju, Korea (**Oral**) [Excellent Paper Award - Oral Presentation].

(8) Jeong, S.; Baig, C. The Molecular Origin of the Stress Relaxation of the Polymer Melts after the Cessation of Steady Shear Flow. 04/2018, The Polymer Society of Korea, Daejeon, Korea (**Oral**) [Excellent Oral Presentation Award (English)].

(9) Jeong, S.; Baig, C. Influence of Closed-loop Conformation of the Polymer on the Interfacial Molecular Mechanisms under Shear Flow. 06/2018, The 7th Pacific Rim Conference on Rheology 2018, Jeju-island, Korea (**Oral**).

(10) Jeong, S.; Baig, C. Molecular Characteristics of Stress Relaxation of Polymer Melts upon Cessation of Steady Shear via Molecular Dynamics Simulation. 10/2018, The Korean Institute of Chemical Engineers Fall Symposium 2018, Daegu, Korea (**Oral**) [Hoemyeong Graduate Research Award].

(11) Jeong, S.; Baig, C. 전단 유동의 급정지(Cessation of Steady Shear flow) 아래 고분자 용융체(polymer melts)의 응력 완화(Stress Relaxation) 현상 분석. 11/2018, The Korean Society of Rheology 2018, Daejeon, Korea (**Poster**).

3. Honors and Awards

(1) UNIST Interdisciplinary Project Best Poster Award, Ulsan National Institute of Science and Technology, 2013. 11. 04.

(2) WISET Young Women Researcher Award, The Korean Institute of Chemical Engineers, 2016. 04. 29.

(3) SPE Korea Hyun Gun Sup Award, SPE Korea, 2017. 06. 30.

(4) Excellent Oral Presentation Award, The Korean Institute of Chemical Engineers, 2017. 10. 27.

(5) Excellent Paper Award - oral presentation, The Korean Society of Rheology, 2017. 11. 17.

(6) Excellent Oral Presentation Award (English), The Polymer Society of Korea, 2018. 04. 06.

(7) Hoemyeong Graduate Research Award, The Korean Institute of Chemical Engineers, 2019. 04. 26.